JUNO 水相实验中的太阳中微子观测研究

**Research on Solar Neutrino Observation
with JUNO Water Phase**

(申请清华大学理学博士学位论文)

培 养 单 位： 工程物理系

学　　　科： 物理学

研 究 生： 翁　　俊

指 导 教 师： 续 本 达　副教授

二〇二五年八月

Research on Solar Neutrino Observation with JUNO Water Phase

Dissertation submitted to

Tsinghua University

in partial fulfillment of the requirement

for the degree of

Doctor of Philosophy

in

Physics

by

Weng Jun

Dissertation Supervisor : Associate Professor, Xu Benda

August, 2025

TABLE OF CONTENTS

CHAPTER 1 INTRODUCTION

CHAPTER 2 THE JUNO DETECTOR

The Jiangmen Underground Neutrino Observatory (JUNO) is a multipurpose neutrino experiment under construction in southern China. The primary scientific objective of JUNO is to determine the neutrino mass ordering and precisely measure neutrino oscillation parameters by detecting reactor antineutrinos from the Yangjiang and Taishan nuclear power plants, located approximately 53 km from the JUNO site. The JUNO detector consists of a central detector (CD) containing 20 kilotons of liquid scintillator (LS), a water Cherenkov detector (WCD) serving as a cosmic muon veto, and a top tracker (TT) for additional muon tracking. The CD is housed within a large acrylic sphere with a diameter of 35.4 m, which is further enclosed by a stainless steel lattice structure. The WCD surrounds the CD and is filled with 35 kilotons of ultrapure water, while the TT is positioned above the WCD. The entire detector assembly is situated approximately 700 m underground, equivalent to 1800 m of water overburden, to mitigate cosmic ray interference.

CHAPTER 3 THE PMT CALIBRATION IN WATER PHASE

3.1 The single electron response of MCP-PMTs

The photomultiplier tubes (PMT) see extensive deployments in particle physics, particularly neutrino experiments. A PMT comprises a photocathode, an electron multiplier, an anode, and other necessary structural components[1]. Photons from a light source incident on the photocathode follow a Poisson process. Some of them are converted to photoelectrons (PE) via the photoelectric effect and such PEs enter the multiplier[2]. Those two processes are Bernoulli selections, with the probabilities known as the *quantum efficiency* (QE) and the *collection efficiency* (CE). The PE count (n_{PE}) in a specific time interval follows a Poisson distribution[3].

The electron amplification is driven by the secondary electron emission (SEE). When an incident particle, such as electron and ion, collides with or goes through a solid surface, one or more secondary electrons are emitted[4]. The average number of secondaries produced per incident particle is the secondary-emission yield (SEY, δ). The energy distribution of the secondaries ($d\delta/dE$) is related to the energy of the incoming particle, the incident angle, the target material, etc.[5]. Bruining and Boer[6], Ushio et al.[7] and Jokela et al.[8] conducted target-shooting experiments using electron guns, and measured the SEY in the current mode. Olano and Montero[9] measured the energy distribution $d\delta/dE$ of Kapton, Teflon, and Ultem by charging analysis, and found the energy of secondaries to be much smaller than that of the primary electrons. Such results are then extrapolated to PMTs[10-11]. The low light intensity at which a PMT operates makes the incident electrons discrete. Therefore, one should be careful when extending the SEY from the current mode to a single electron case, the pulse mode.

While being amplified by the multiplier, a single PE induces numerous electrons, which are captured by the anode within a few hundred picoseconds. The initial energy of the PEs produced at the photocathode is $\sim 1\,\text{eV}$[12]. The potential difference between the photocathode and the multiplier dominates the incident energy of the PEs arriving at the multiplier. Therefore, the amplifier provides nearly identical gain for the PEs. Because the total charge of the electrons captured by the anode is typically described by a Gaussian distribution in light of the central limit theorem of probability, the probability density function (PDF) of the single electron response (SER) charge distribution is $f_{\mathcal{N}}(Q; Q_1, \sigma_1^2)$,

where Q_1 is the mean charge, and σ_1 is its standard deviation. The PE count n_{PE} follows a Poisson distribution with the probability mass function $P_\pi(n_{PE}; \lambda)$, where λ is the expected PE count at a certain light intensity. After amplification, the total charge distribution $f(Q)$ is a folding of the Poisson distribution and the SER charge distribution[3]. There are two types of background processes. The first one follows a low-charged finite-width Gaussian $\mathcal{N}(0, \sigma_0^2)$ without any PEs emitted from the photocathode. The second process is discrete with a probability w. Examples include thermoemission and noise generated by incident light. This discrete process follows an exponential distribution $\text{Exp}(\alpha)$, with α being the rate of exponential decay. Considering the charge distribution of the two types of background processes being $f_b(Q)$, the overall charge distribution can be expressed in Eq. (3.1):

$$
\begin{aligned}
f(Q) =& P_\pi(n_{PE} = 0; \lambda)f_b(Q) + \sum_{n_{PE}=1}^{\infty} P_\pi(n_{PE}; \lambda)f_\mathcal{N}(Q; n_{PE}Q_1, n_{PE}\sigma_1^2) \\
\approx& \left\{ \frac{(1-w)}{\sigma_0\sqrt{2\pi}} \exp\left(-\frac{Q^2}{2\sigma_0^2}\right) + w\theta(Q) \times \alpha\exp\left(-\alpha Q\right) \right\} e^{-\lambda} \\
&+ \sum_{n_{PE}=1}^{\infty} \frac{\lambda^{n_{PE}}e^{-\lambda}}{n_{PE}!} \times \frac{1}{\sigma_1\sqrt{2\pi n_{PE}}} \times \exp\left(-\frac{\left(Q - n_{PE}Q_1\right)^2}{2n_{PE}\sigma_1^2}\right)
\end{aligned} \tag{3.1}
$$

where $\theta(Q)$ is the Heaviside function. When λ is less than 0.1, the probability of observing two or more PEs is less than one-tenth of the probability of observing a single PE. In this case, the charge distribution will only show the peak of the pedestal ($Q = 0$) and the peak of the single PE ($Q = Q_1$) as indicated in the blue histogram in Fig 3.1. We can obtain an approximate SER charge spectrum after applying some cuts to remove the pedestal. Our work aligns different PMTs' gain by dividing the SER charge spectrum with Q_1 as Q/Q_1. Instead of a large-sized dynode-chain commonly used in PMTs, MCP-PMTs employ MCPs as electron multipliers. MCP-PMTs are currently in use or planned for neutrino experiments like the Jiangmen Underground Neutrino Observatory (JUNO)[14] and the Jinping Neutrino Experiment[13], collider experiments like the Belle II TOP detector[15] and the PANDA DIRC Cherenkov detector at FAIR[16], and cosmic ray observatories like the Large High Altitude Air Shower Observatory[17]. Initially, the fact that the feedback ions cause damage to the photocathode led to a lifetime issue of MCP-PMTs[18].

The atomic layer deposition (ALD) technique[10] is applied to fabricate MCP-PMTs solving the lifetime issue[19]. Chen et al.[2] indicated that depositing high SEY materials such as Al_2O_3 via ALD on the input electrode of the first MCP can enhance the probability
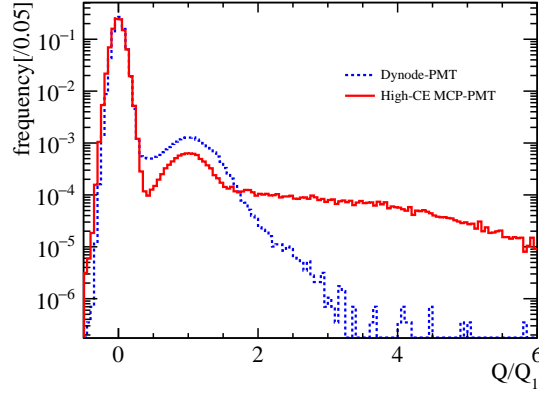
Figure 3.1 The charge spectrum of the high-CE MCP-PMT GDB-6082 (red) and a dynode-PMT (blue)[13]. The blue histogram consists of the pedestal $Q = 0$ and the principal peak of $Q = Q_1$, while the red histogram includes jumbo charges.

of collecting the secondaries to improve CE to nearly 100 % rather than being constrained by the MCP open-area ratio. This enhancement is later extended to a composite Al_2O_3-MgO layer by Cao et al.[20] and Zhang et al.[21] to allow for increased gain, improved single electron resolution, and a higher peak-to-valley ratio of the MCP-PMTs[11].

In the performance tests to evaluate the 8-inch high-CE MCP-PMT by the Jinping Neutrino Experiment, *jumbo charges* are found in the SER charge spectra[13], as shown in the red histogram in Fig 3.1. Similar charges have also been observed in the mass testing of the 20-inch MCP-PMTs at JUNO, identified as the "long tail" in the SER charge distribution[22]. Orlov et al.[23] reported that the pulse height distribution of the high-CE MCP-PMTs had a non-Gaussian long-tail structure. Zhang et al.[24] used the charge model in Eq. (3.1) for the jumbo charges and recommended an extra gain calibration. Yang et al.[25] conducted a voltage-division experiment to reveal that the MCP gain for the low-energy electrons is significantly smaller than that for the high-energy ones. Thus, the MCP gain for the secondaries differs from that for the PEs entering the channels directly. The SER charge model in Eq. (3.1) is no longer sufficient to accurately calibrate this type of PMT. Understanding the origin of the jumbo charges is necessary for an appropriate SER charge calibration.

To elucidate the nature of the jumbo charges, the Gamma distribution is introduced and a voltage-division experiment is developed to measure the relationship between MCP gain and the energy of the incident electrons. Considering the SEE model, we elucidate the nature of the jumbo charges and calculate the total SEY of the Al_2O_3-MgO layer when the incident energy is $650\,eV$. Through convolution-based modeling, the physical mechanisms driving have been clarified, and a quantitative mathematical framework establishe,

which is the first formulation for these kind of high-CE MCP-PMTs.

3.1.1 Gamma-Distributed SER charges

Every multiplication of electrons at the dynodes or MCP channels follows approximately a Poisson distribution[26]. A series of such multiplications forms cascaded Poissonians[1] and is an example of the branching process[27] challenging to perform analytical computations. Woodward[28] argued that the SER charge spectrum exhibits an intermediate shape between a Poisson and a Gaussian. Prescott[29] proposed a cascaded Polya distribution to characterize the electron multiplication in PMT, particularly when considering the non-uniformity of the dynode surface. Kalousis[30-31] approximated the Polya distribution as a Gamma one to calibrate PMT and achieved better results than the Gaussian model in Eq. (3.1).

Instead of the Gaussian containing a small nonphysical tail less than 0, we choose a Gamma distribution $\Gamma(\alpha, \beta)$ defined by the scale factor α and the rate factor β, as shown in Eq. (3.2):

$$f_\Gamma(x; \alpha, \beta) = \frac{x^{\alpha-1} e^{-\beta x} \beta^\alpha}{\Gamma(\alpha)} \quad \text{for } x > 0 \quad \alpha, \beta > 0 \tag{3.2}$$

where $\Gamma(\alpha)$ is the Gamma function. A Gamma distribution is uniquely determined by its expectation value $\alpha/\beta = Q_1$ and variance $\alpha/\beta^2 = \sigma_1^2$, which can be converted into the Gaussian counterparts in Eq. (3.1). The charge spectrum based on the Gamma distribution is,

$$f(Q) = P_\pi(n_{\text{PE}} = 0; \lambda) f_{\text{b}}(Q) + \sum_{n_{\text{PE}}=1}^{\infty} P_\pi(n_{\text{PE}}; \lambda) f_\Gamma(Q; n_{\text{PE}}\alpha, \beta). \tag{3.3}$$

3.1.2 Jumbo Charges through Extra Multiplication

SEE has received considerable attention during the widespread application of electronic tubes. Bruining summarized the SEE's methods, findings, and applications in his classic *Physics and Applications of Secondary Electron Emission*[32]. Baroody[33] put forward his SEE theory of metals assuming that an incident primary electron interacts only with free electrons in the conduction band, without considering the variation of secondary emission with the primary energies. Dekker et al.[34] presented the SEE quantum theory of the Coulomb interaction between the incident primaries and the lattice electrons. Wolff[35] provided the cascade theory for the diffusion, the energy loss, and the multiplication of the secondary electrons within a metal. Assuming both incident and back-

scattered electrons within the target are isotropic, Kanaya et al.[36] calculated the SEY from insulators with the ionization potential by setting the valence electron and the back-scattered coefficient besides the parameter of the free-electron density effect. Vaughan[37] formulated the SEY as a function of impact energy and direction used in computer programs, known as the *Vaughan model*. Furman and Pivi[5] developed a mathematically self-consistent Monte Carlo program to elucidate the SEE phenomenon from solid surfaces usually called the *Furman model*. This model incorporates the statistical nature of the SEE process by considering the probability distribution governing the number of the secondaries emitted per incident primary electron. The energies of secondary electrons are approximated as independent and identically distributed random variables determined by the material properties and the primary energies.

Early models primarily focused on theoretical explanations of SEE. The Vaughan and Furman models emphasize the Monte Carlo computation instead. Comparatively, the Furman model strives for physical consistency and better agreement with experiments. Therefore, we choose it for more adjustable parameters and higher accuracy.

3.1.2.1 Furman probabilistic model

In the Furman model[5], there are three kinds of secondary electrons. The first is the back-scattered electron, emitted through elastic scattering on the surface of the target material. The energy distribution $\mathrm{d}\delta_{\mathrm{bs}}/\mathrm{d}E$ is defined in Eq. (3.4), where δ_{bs} is the yield of the back-scattered electron, the Heaviside function $\theta(E)$ ensures the $E < E_0$. E_0 is the incident energy of the primary electron, θ_0 is the incident angle, and σ_{bs} is an adjustable standard deviation.

$$\frac{\mathrm{d}\delta_{\mathrm{bs}}}{\mathrm{d}E} = \theta(E)\theta\left(E_0 - E\right)\delta_{\mathrm{bs}}\left(E_0, \theta_0\right)\frac{2\exp\left(-\left(E - E_0\right)^2/2\sigma_{\mathrm{bs}}^2\right)}{\sqrt{2\pi}\sigma_{\mathrm{bs}}\operatorname{erf}\left(E_0/\sqrt{2}\sigma_{\mathrm{bs}}\right)} \tag{3.4}$$

After penetrating the target material, some electrons are inelastically scattered by the atoms and are reflected out to form the second category. Lenard called the bending of the electron track "diffusion", and the trajectory turning 90° as "Rückdiffusion" in German literature[32]. Furman and Pivi[5] adopted this convention to name them as the *rediffused electrons*. The energy distribution of the rediffused electrons is defined as Eq. (3.5), where δ_{rd} is the yield of rediffused electron, and q is an adjustable parameter.

$$\frac{\mathrm{d}\delta_{\mathrm{rd}}}{\mathrm{d}E} = \theta(E)\theta\left(E_0 - E\right)\delta_{\mathrm{rd}}\left(E_0, \theta_0\right)\frac{(q + 1)E^q}{E_0^{q+1}} \tag{3.5}$$

The final and most important kind is the true-secondary electrons. Upon deeper penetration of electrons into the target material, intricate physical processes ensue, generating one or more secondaries. This is the process of multiplying electrons. The spectrum is defined as Eq. (3.6).

$$\frac{\mathrm{d}\delta_{ts}}{\mathrm{d}E} = \sum_{n=1}^{\infty} \frac{n P_{n,ts}\left(n; \delta_{ts}(E_0, \theta_0)\right) \left(E/\epsilon_n\right)^{p_n-1} e^{-E/\epsilon_n}}{\epsilon_n \Gamma\left(p_n\right) \Upsilon\left(np_n, E_0/\epsilon_n\right)} \times \Upsilon\left[(n-1)p_n, \left(E_0 - E\right)/\epsilon_n\right] \quad (3.6)$$

where $\delta_{ts}(E_0, \theta_0)$ is the yield of the true-secondary electrons when the incident energy is E_0 and the incident angle is θ_0, $\epsilon_n > 0$ and $p_n > 0$ are the phenomenological parameters. $\gamma(z, x)$ is the incomplete gamma function, and $\Upsilon(z, x) = \gamma(z, x)/\Gamma(z)$ is the normalized form satisfying $\Upsilon(0, x) = 1$. n, the number of the true-secondary electrons, follows a Poisson distribution $(\delta_{ts}(E_0, \theta_0))$. $P_{n,ts}$ is its probability mass function.

As illustrated in Fig. 3.2, we set the parameters as $\delta_{bs} = 0.05$, $\delta_{rd} = 0.5$, $\delta_{ts} = 5$[11], $\theta_0 = 0°$ and $E_0 = 650\,\mathrm{eV}$. The total spectrum is $\mathrm{d}\delta/\mathrm{d}E = \mathrm{d}\delta_{bs}/\mathrm{d}E + \mathrm{d}\delta_{rd}/\mathrm{d}E + \mathrm{d}\delta_{ts}/\mathrm{d}E$. The energies of the secondaries are usually less than $100\,\mathrm{eV}$ when the incident energy E_0 is $650\,\mathrm{eV}$.
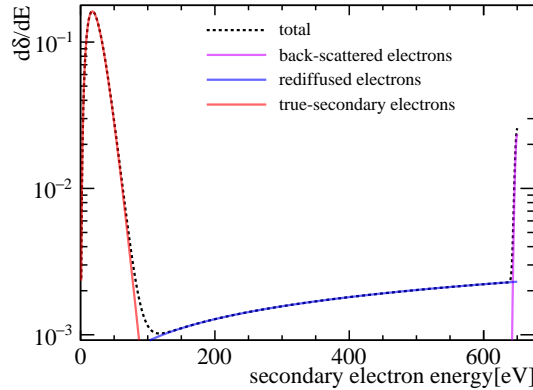

Figure 3.2 The total energy spectrum of the secondary electrons when the incident energy is $650\,\mathrm{eV}$. The violet, blue, and red lines represent $\mathrm{d}\delta_{bs}/\mathrm{d}E$, $\mathrm{d}\delta_{rd}/\mathrm{d}E$, and $\mathrm{d}\delta_{ts}/\mathrm{d}E$, repectively. The black dashed line is $\mathrm{d}\delta/\mathrm{d}E$.

3.1.2.2 An extra multiplication mode

The MCP-PMT under study uses a Chevron stack of two MCPs as the electron multiplier. As shown in Fig. 3.3, an Al_2O_3-MgO-Al_2O_3 layer[21] is deposited on the channel surface of the lead glass body and on the entrance electrode M1 of the first MCP through the ALD technology. There are two alternative routes of amplification for every PE: the *channel mode*, where the PE directly enters a channel, and the *surface mode*, where the

secondaries from M1 enter the MCP channels under the focusing electric field. The selection of these two routes is a Bernoulli trial[1].

The MCP gain for those low-energy secondaries in the surface mode is substantially smaller than that for the primary PEs in the channel mode[10].

3.1.2.3 Voltage-division Experiment

The dependence of the MCP gain for an electron versus its incident energy at the channel entrance is crucial to understanding the jumbo charges. We designed a voltage-division experiment to measure such a relationship.

As shown in Fig 3.3, we utilized a positive high-voltage power supply (positive HV) to stabilize the potentials applied to the MCPs through the circuit[38]. In parallel, we took a negative high-voltage power supply (negative HV) to vary the electric potential difference between the photocathode and M1 to get PEs at different incident energies. Compared to the experiment of Yang et al.[25] where the potentials of all the electrodes M1-4 are controllable, our design is a simplified adaptation only to tune the energies of the PEs with commercially available HV products.

We used a picosecond laser with a wavelength of 405 nm to illuminate the MCP-PMT at 1 kHz rate and feed an electronic trigger signal to capture waveform data. To obtain the single PE, we adjusted the intensity of the laser until the occupancy was below 0.1. We deployed a 10-bit oscilloscope (HDO9000 with HD1024 Technology)[39] to capture the 100 ns waveform with a sampling rate of 40 GS/s and a range of [-20, 60] mV.

We obtained the gain of the MCP-PMTs at different energies of the incident electrons by fitting the Gaussian on the charge distribution, and conducted the same experiment on two MCP-PMTs with (Fig. 3.4(b)) and without (Fig. 3.4(a)) Al_2O_3-MgO deposited on M1 to contrast the effect of the surface mode. The positive voltages for the MCP-PMT with and without Al_2O_3-MgO on M1 are +1205 V and +1240 V, respectively. The initial energies of the PEs are ~1 eV[12] and the systematic error of the negative HV itself is within 2 V. The incident energies (E_0) are defined as the energies acquired by the PEs in the electric field, numerically equal to the potential difference between the photocathode and M1, with an error of ±2 eV. We scanned the MCP gain and measured it every 10 eV when $10 \leqslant E_0 < 100$ eV, every 20 eV when $100 \leqslant E_0 < 200$ eV and every 50 eV when $200 < E_0 \leqslant 650$ eV. For the MCP-PMT with Al_2O_3-MgO deposited on M1, our scan range is $10 \leqslant E_0 \leqslant 600$ eV. For the MCP-PMT without, the range is $10 \leqslant E_0 \leqslant 680$ eV.

The charges of the captured waveforms were measured with *fast stochastic matching*
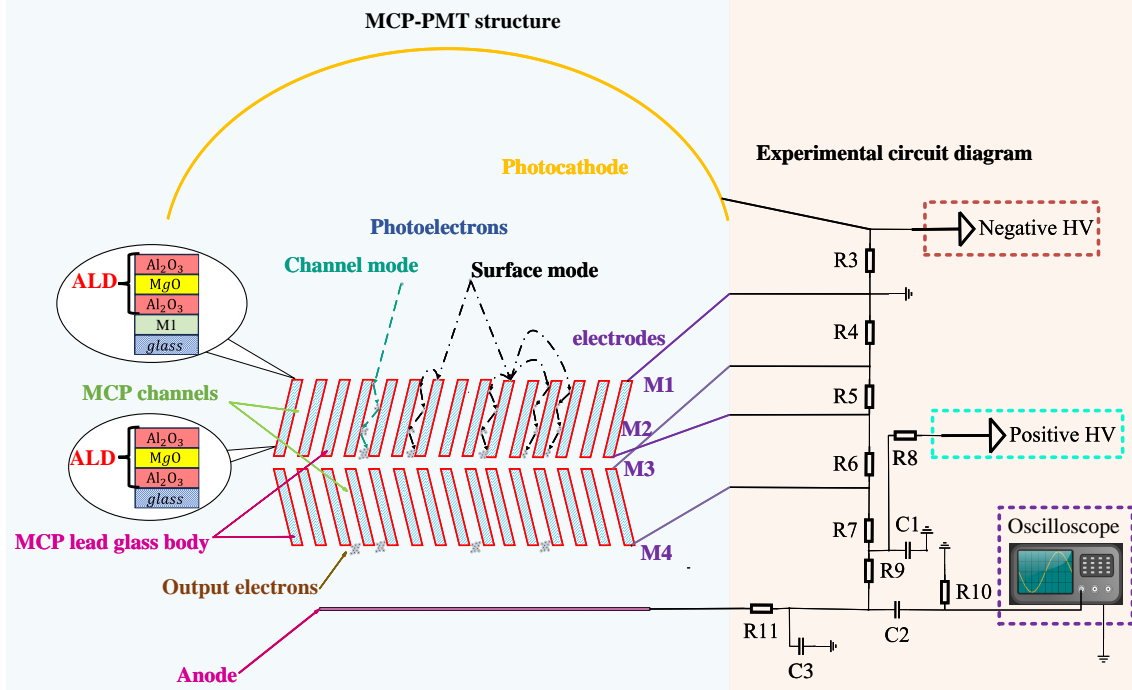
Figure 3.3   M1 and M3 are the input electrodes of MCPs, M2 and M4 are the output electrodes, and the four electrodes provide the potential differences during operation. The PEs directly enter the channels (channel mode) or hit M1 to produce secondary electrons that enter the channels later (surface mode)[2]. After entering the MCP channel, the electron collides with the channel wall many times and is amplified in a series of such multiplications[1]. Our circuit design was modified from the circuit implementation in the reference[38]. We removed useless R1 and R2 in our circuit design, while the rest of the resistors remained unchanged.

pursuit (FSMP)[40-41], which suppresses the interference of electronic noise to give accurate charge spectra under a wide range of gain. Due to FSMP's ability to count PEs, the charge would be 0 when $n_{PE} = 0$ and the pedestal is cleanly cut out in the output charge distribution. In Fig. 3.4, the peaks are attributed to the channel mode. The jumbo charges from the surface mode are to the right and deficient amplifications are to the left of the peaks. Due to the small contribution of secondaries from the surface mode for the MCP-PMT without Al_2O_3-MgO deposited on M1, there is no jumbo charge in the charge spectrum, as shown in Fig. 3.4(a). To obtain the MCP gain for the electrons directly entering the channels, we only fitted the peak to exclude the influence of the surface mode.

We obtained approximate values of μ_p and σ_p of the charge distribution to provide initial values and ranges for a detailed fit. The fit ranges were determined from the incident energies of the PEs, when $E_0 > 100$ eV, it was $[\mu_p - 1.3\sigma_p, \mu_p + 1.6\sigma_p]$; when $30 < E_0 \leqslant 100$ eV, $[\mu_p - 0.8\sigma_p, \mu_p + 1.6\sigma_p]$; and when $E_0 \leqslant 30$ eV, $[\mu_p - 1.5\sigma_p, \mu_p + 1.8\sigma_p]$. It is sufficient to extract the mean charge $\mu(E_0)$ and the standard deviation $\sigma(E_0)$ of the channel-mode peak to measure the MCP gain for electrons at different energies.
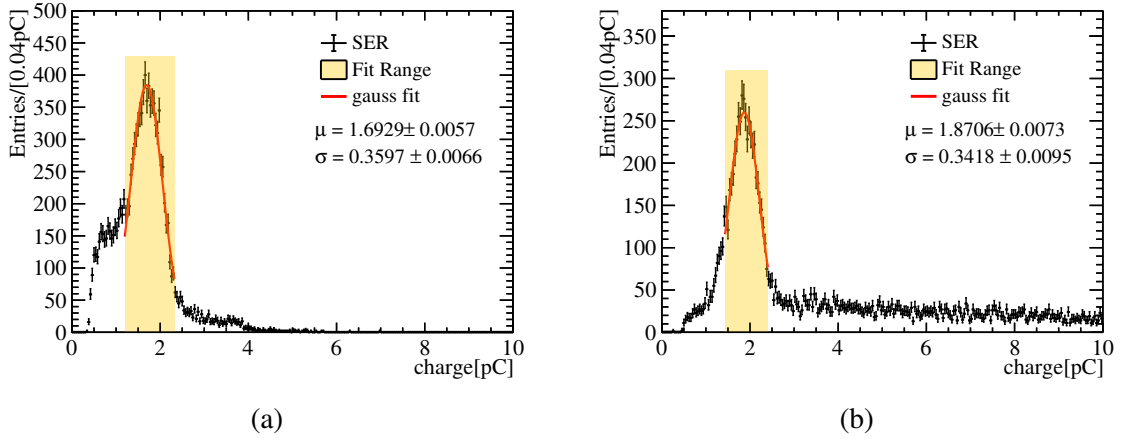
(a)   (b)

Figure 3.4   Fit of the charge spectrum of the MCP-PMT without (a) and with (b) Al_2O_3-MgO deposited on M1. We observed that (a) does not exhibit jumbo charges. The yellow areas are incident energy-dependent intervals and the red lines are fitting results of the Gaussian functions in the intervals.

After fitting with Gaussians, we interpolate and extrapolate linearly to obtain the relations of $\mu(E_0)$ and $\sigma(E_0)$ in Fig. 3.5. The difference in the relations of MCP-PMTs with and without Al_2O_3-MgO deposited on M1 comes from the influence of the charge contributed from the surface mode. When $E_0 < 200\,eV$, $\mu(E_0)$ rapidly increases. As $E_0 > 200\,eV$, $\mu(E_0)$ gradually stabilizes. The $\sigma(E_0)$ is overall increasing similar to $\mu(E_0)$ but sees a drop around 200 eV. A similar trend of $\mu(E_0)$ is reported by Yang et al.[25]. In our case, the best relative resolution σ/μ is at around 600 eV and Yang et al.'s results suggested 200 eV. Cao et al.[20] found that the SEY of Al_2O_3-MgO increases with the incident energy in 100–600 eV. Even though the film structure and thickness we used are different, we can still make a rough assessment that the trend of σ/μ obtained here is reasonable, considering the variation curves of the SEY of Al_2O_3 and MgO with energy.

3.1.2.4 Charge-Spectra Decomposition

The Furman model in Sec. 3.1.2.1 predicts the energies of the secondaries. Our voltage-division experiment in Sec. 3.1.2.3 measured the relationship between the MCP gain and the incident energies of the electrons. We follow the flowchart in Fig. 3.6 to calculate the charge distribution by Monte Carlo. In this study, we shone the laser at the apex of the photocathode hemisphere, and the PEs hit M1 with an incident angle $\theta_0 = 0°$. The complex amplification process in the channels is described by the incident energy-dependent Gamma distributions $\Gamma(\alpha(E), \beta(E))$ described in Sec. 3.1.1. The $\alpha(E)$ and $\beta(E)$ are estimated with the relations of $\mu(E)$ and $\sigma(E)$ of MCP-PMT without Al_2O_3-MgO coating on the input electrode, which eliminates the influence of the surface mode.
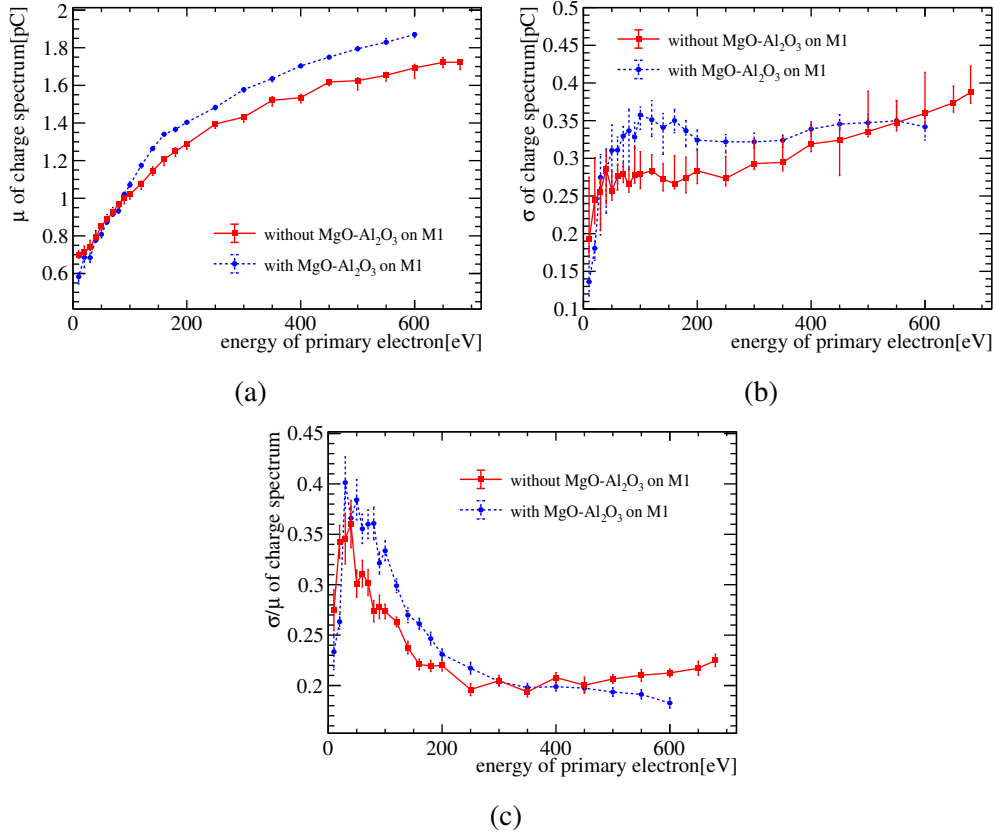
11

(a)

(b)

(c)

Figure 3.5　(a) The mean μ increases as the incoming electron energy E_0 increases. (b) The standard deviation σ changes with energy. The MCP-PMT with Al_2O_3-MgO deposited on M1 (the red line) shows a similar variation trend to the one without (the blue line). (c) The resolution σ/μ increases between 0-50 eV, decreases between 50-400 eV, and after 400 eV, there is a slight decrease for those with Al_2O_3-MgO deposited on M1 (the blue line) and a slight increase for those without (the red line).

Taking into account the light intensity, we repeatedly sample n_{PE} from the Poisson distribution and sum up n_{PE} SER charges for the output to get a spectrum.

For sampling an SER charge, we assign the probabilities of the channel and surface modes as p and $1 - p$ for a Bernoulli trial. The SER charge spectrum $f_{MCP-PMT}(Q)$ is

$$f_{MCP-PMT}(Q) = p f_{ch}(Q) + (1 - p) f_{surf}(Q) \tag{3.7}$$

where $f_{ch}(Q)$ and $f_{surf}(Q)$ are the charge distributions of the channel and surface modes. $f_{ch}(Q)$ is set to $f_\Gamma(Q; \alpha(E_0), \beta(E_0))$, with the incident energy being 650 eV. The factors $\alpha(E_0), \beta(E_0)$ are converted from $\mu(E_0)$ and $\sigma(E_0)$ without Al_2O_3-MgO coating in Fig. 3.5.

The $f_{surf}(Q)$ is divided into three components by the Furman model corresponding to Eqs. (3.4)–(3.6), $f_{bs}(Q)$ for the back-scattered electrons, $f_{rd}(Q)$ for the rediffused elec-

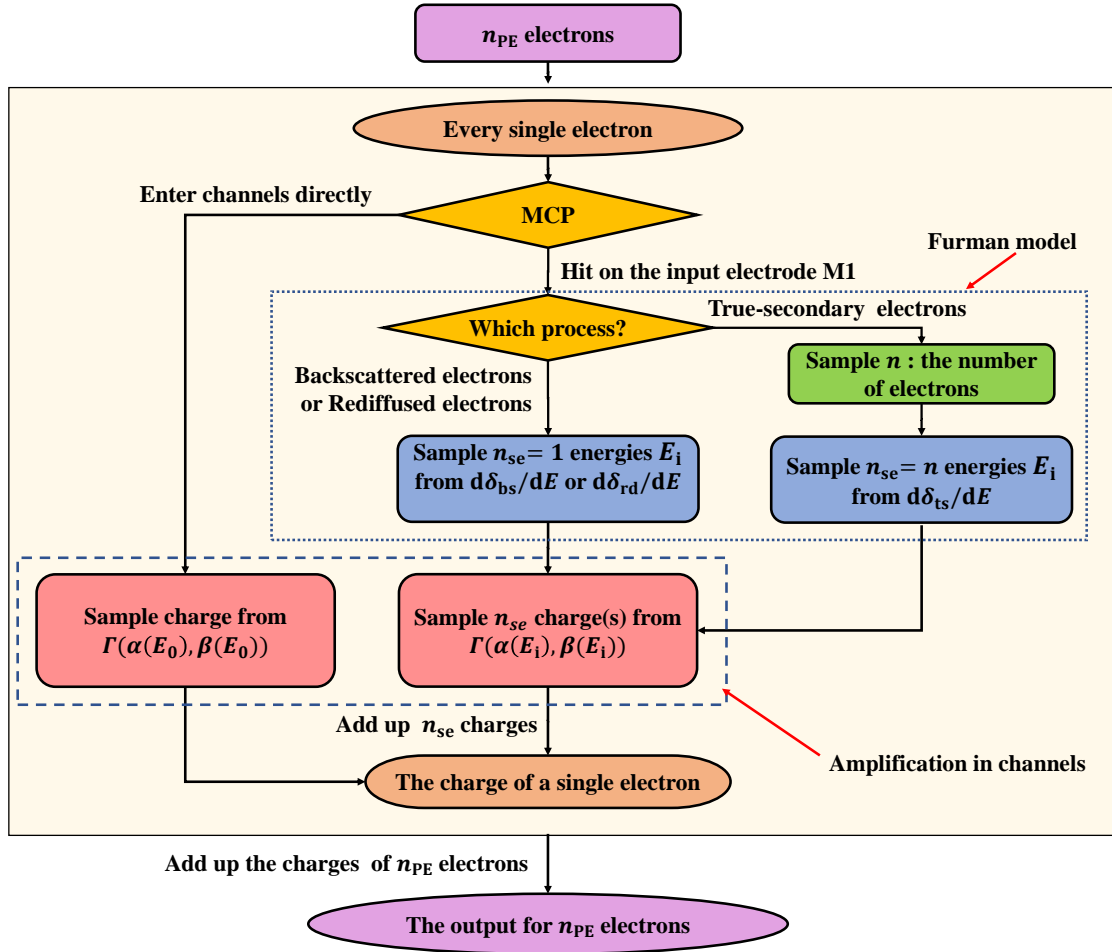Figure 3.6   The flowchart of Monte Carlo to compute the charge spectrum. The output charge consists of n_{PE} SER charges. The PEs in the channel mode enter channels directly, while PEs in the surface mode hit the input electrode. The energies of the n_{se} secondaries in the surface mode are sampled from the Furman model. The amplification in channels is modeled by the incident energy-dependent Gamma distribution.

trons, and $f_{\mathrm{ts}}(Q)$ for the true-secondary electrons.

$$
\begin{aligned}
f_{\mathrm{surf}}(Q) &= p_{\mathrm{bs}} f_{\mathrm{bs}}(Q) + p_{\mathrm{rd}} f_{\mathrm{rd}}(Q) + (1 - p_{\mathrm{bs}} - p_{\mathrm{rd}}) f_{\mathrm{ts}}(Q) \\
&= \delta_{\mathrm{bs}} f_{\mathrm{bs}}(Q) + \delta_{\mathrm{rd}} f_{\mathrm{rd}}(Q) + (1 - \delta_{\mathrm{bs}} - \delta_{\mathrm{rd}}) f_{\mathrm{ts}}(Q)
\end{aligned}
\tag{3.8}
$$

where p_{bs} and p_{rd} are the mixture ratios determined by the composition and thickness of surface emissive material that varies among the PMTs. Furman and Pivi[5] assume that only one electron is emitted in back-scattered mode and rediffused mode so that $\delta_{\mathrm{bs}} = p_{\mathrm{bs}}$ and $\delta_{\mathrm{rd}} = p_{\mathrm{rd}}$. In the calculation, we specify $\delta_{\mathrm{rd}} = 0.09$ and $\delta_{\mathrm{bs}} = 0.01$. The energy of the back-scattered electron is nearly equal to that of the PEs in the channel mode, and so is the MCP gain for them. The energy of the rediffused electron is lower – from $100\,\mathrm{eV}$ to $600\,\mathrm{eV}$, causing the charge after MCP multiplication to be slightly smaller thanks to the relatively slow increase of gain in that range in Fig. 3.5(a). Either contributes a single

13

electron and is practically indistinguishable from the channel mode in the charge spectra. Such a degeneracy is summarized in Eq. (3.9):

$$
\begin{aligned}
f_{\text{MCP-PMT}}(Q) &= p f_{\text{ch}}(Q) + (1-p) f_{\text{surf}}(Q) \\
&= p f_{\text{ch}}(Q) + (1-p)[\delta_{\text{bs}} f_{\text{bs}}(Q) + \delta_{\text{rd}} f_{\text{rd}}(Q) + (1 - \delta_{\text{bs}} - \delta_{\text{rd}}) f_{\text{ts}}(Q)] \\
&= [p + (1-p)(\delta_{\text{bs}} + \delta_{\text{rd}})] f_{\text{ch}}(Q) + (1-p)(1 - \delta_{\text{bs}} - \delta_{\text{rd}}) f_{\text{ts}}(Q)
\end{aligned}
$$
(3.9)

where the spectra $f_{\text{ch}}(Q)$, $f_{\text{rd}}(Q)$ and $f_{\text{bs}}(Q)$ are merged into $f_{\text{ch}}(Q)$.

Nevertheless, Eq. (3.9) is incomplete. We should consider the case when the secondaries hit the MCP surface again. The round trip does not inject extra energy. A back-scattered or rediffused secondary gets amplified essentially in the same way as a primary PE, while a true-secondary electron has too low energy to multiply again. Therefore, p_0, the net contribution to $f_{\text{ch}}(Q)$, is a geometric series

$$
p_0 = p \sum_{i=0}^{\infty} [(1-p)(\delta_{\text{bs}} + \delta_{\text{rd}})]^i = \frac{p}{1 - (1-p)(\delta_{\text{bs}} + \delta_{\text{rd}})}
$$
(3.10)

and $f_{\text{ts}}(Q)$ gets $\frac{(1-p)(1-\delta_{\text{bs}}-\delta_{\text{rd}})}{1-(1-p)(\delta_{\text{bs}}+\delta_{\text{rd}})}$ or $1 - p_0$. Eq. (3.9) is remarkably reduced to

$$
f_{\text{MCP-PMT}}(Q) = p_0 f_{\text{ch}}(Q) + (1 - p_0) f_{\text{ts}}(Q).
$$
(3.11)

In the case of the true-secondary electrons, their count n follows a Poissonian. The sum of the sampled n charges serves as the output Q_{ts},

$$
\begin{aligned}
Q_{\text{ts}} &= \sum_{i=1}^{n} Q_i \\
n &\sim \ (\delta'_{\text{ts}}) \\
Q_i &\sim \Gamma[\alpha(E_i), \beta(E_i)]
\end{aligned}
$$
(3.12)

where E_i are sampled from Eq. (3.6). $\alpha(E_i)$ and $\beta(E_i)$ are converted from $\mu(E_i)$ and $\sigma(E_i)$ of Fig. 3.5. For completeness, $\delta_{\text{ts}} = (1 - \delta_{\text{bs}} - \delta_{\text{rd}})\delta'_{\text{ts}}$ is the electric-current ratio of the true-secondary electrons to that of the primary.

The charge spectra of different n are shown in Fig. 3.7(a). Due to the lower energies of the secondaries, their charges are smaller. It is challenging to distinguish each charge formed at the anode, as multiple secondary electrons enter the MCP channels simultaneously. Bigger n results in a larger charge.

A typical decomposition of the SER charge spectra is shown in Fig. 3.7(b). The jumbo charges, also known as the "long tail", are contributed by the true secondaries from the surface mode.
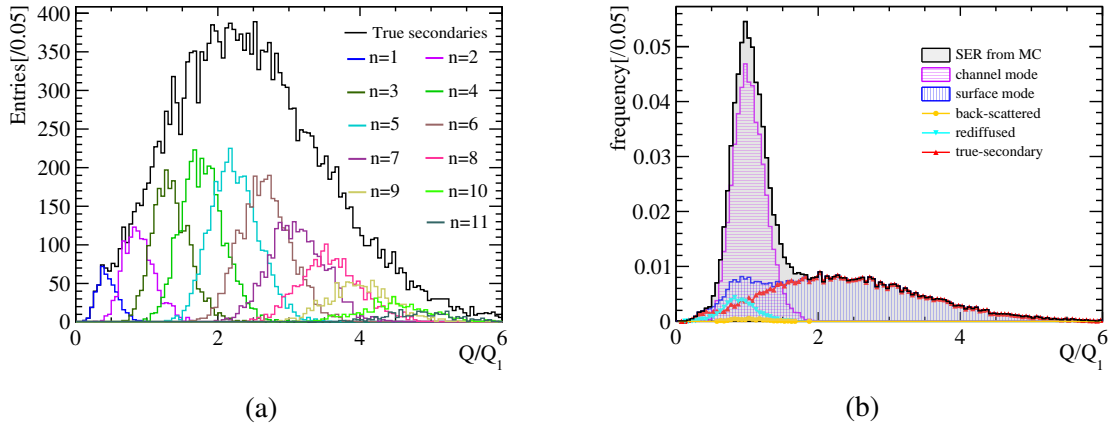
(a)   (b)

Figure 3.7 (a): The charge distribution of the true-secondary electrons mode in the MC calculation when $\delta'_{ts} = 5.5$ and $p_0 = 0.55$. The black histogram gives the sum of all the distributions. (b): The charge distribution formed in the channel mode is concentrated around the peak, while the tail portion is mainly generated by the true-secondary electrons in the surface mode.

3.1.3 Parameter Extraction from Data

It is evident from Eq. (3.11) and (3.12) that δ'_{ts} and p_0 significantly impact the SER charge distribution, demonstrated in Fig. 3.8. We use the MCP-PMT test data by Zhang et al.[13] to determine the two parameters.

(a)   (b)
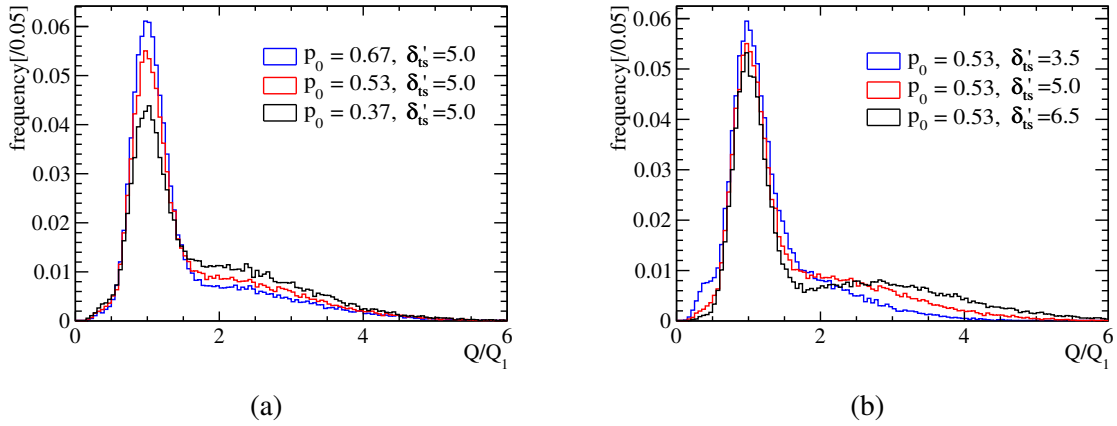
Figure 3.8 δ'_{ts} and p_0 influence the shape of SER charge spectrum from MC. As δ'_{ts} increases, the region of the tail becomes more prolonged. As p_0 increases, the height of the principal peak region increases, and the tail becomes narrower.

Between each pair of predicted and measured charge distributions, we perform a chi-square test. These two histograms are divided into r bins using the same binning method. The entries in the i-th bin are n_i and m_i, adding up to $N = \sum_{i=1}^{r} n_i$ and $M = \sum_{i=1}^{r} m_i$. The chi-square test indicates the similarity between two histograms[42],

$$\chi^2_{r-1} = \sum_{i=1}^{r} \frac{\left(n_i - N\hat{k}_i\right)^2}{N\hat{k}_i} + \sum_{i=1}^{r} \frac{\left(m_i - M\hat{k}_i\right)^2}{M\hat{k}_i} = \frac{1}{MN} \sum_{i=1}^{r} \frac{\left(Mn_i - Nm_i\right)^2}{n_i + m_i} \quad (3.13)$$

15

where $\hat{k}_i = \frac{n_i + m_i}{N + M}$.

The χ^2_{r-1} are scanned in the (p_0, δ'_{ts}) grid, with an example in Fig. 3.9(a). We use a linear model[43] to smooth the approximate parabolic relationship between the χ^2_{r-1} and (p_0, δ'_{ts}), then extract the $(\hat{p}_0, \hat{\delta}'_{ts})$ that minimizes χ^2_{r-1} with intervals at 68.3 % confidence levels[44].
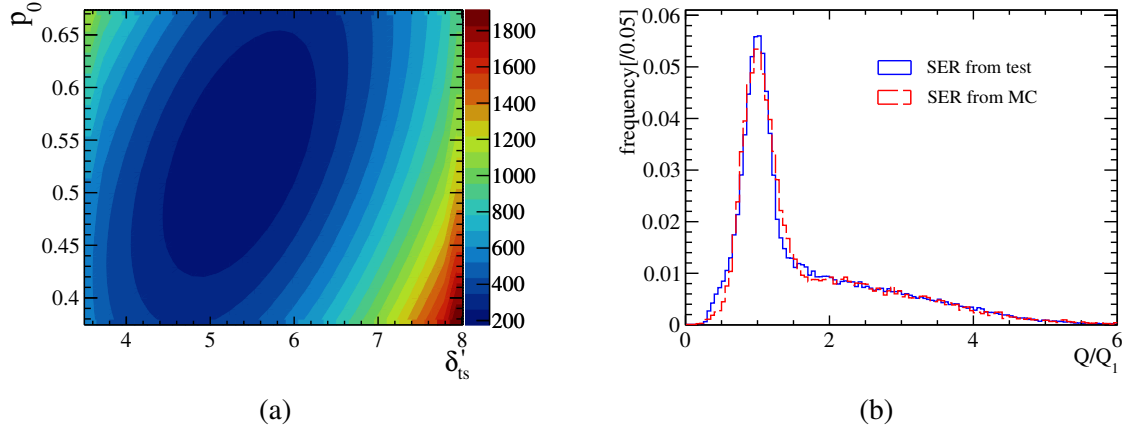

| (a) | (b) |

Figure 3.9   The plot (a) is the contour plot of the chi-square test, with p_0 and δ'_{ts} as parameters and the chi-square values as the height. The plot (b) is an example of the MC histogram (the red line) and the histogram from test (the blue line).

The $\hat{\delta}'_{ts}$ vs. $\hat{p}_0$ scatter plot of 9 MCP-PMTs in Fig. 3.10 does not indicate a strong correlation. They are determined by independent manufacturing stages. On average, δ'_{ts} is 5.979 and p_0 is 0.5341. The PEs of the channel, back-scattered, and rediffused surface modes account for 53.41 %. They constitute the peak. Each of the rest hits the surface to induce 5.979 true-secondary electrons on average.
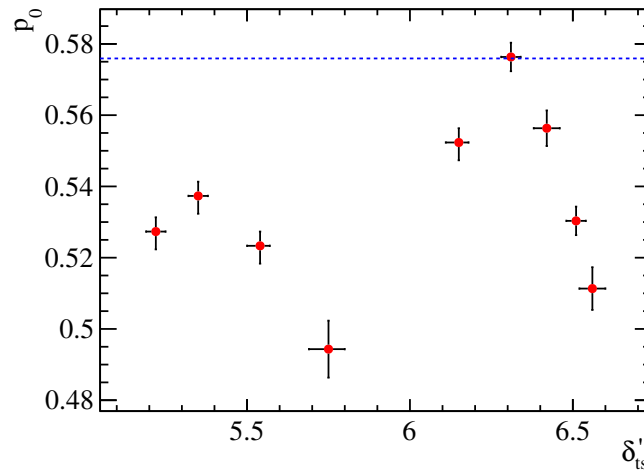

Figure 3.10   When convolving with 9 MCP-PMTs, the distribution of δ'_{ts} and p_0 at the minimum chi-square occurs. The blue dashed line shows the expected $\hat{p}_0$ estimated from[45].

To compare our measurement to previous studies, we convert δ'_{ts} to the SEY δ

$$\delta = \delta_{bs} + \delta_{rd} + (1 - \delta_{bs} - \delta_{rd})\delta'_{ts} \tag{3.14}$$

and the fraction p_0 to p by Eq. (3.10). Cao et al.[20] measured the SEY of Al_2O_3-MgO double-layered film to be 4–5. Chen et al.[2] pointed out that there is an electrostatic lens effect at the MCP channel entrances, making the ratio of the PEs entering the MCP channels smaller than the open-area ratio. When PEs come with an incident angle $\theta_0 = 0°$, the proportion of the PEs directly entering the MCP channels is around 60 % when the MCP open-area ratio is 74.9 %. Chen et al.[45] indicated that the proportion is around 55 % when the open-area ratio is 65 %. The MCPs in our case have pore diameters of 12 m, spacings of 14 m between the pores, and open-area ratios of 66.6 %. The expected $\hat{p}_0 = \frac{55\%}{1-(1-55\%)(\delta_{rd}+\delta_{bs})} \approx 57.6\%$ for $\delta_{rd} + \delta_{bs} = 0.1$.
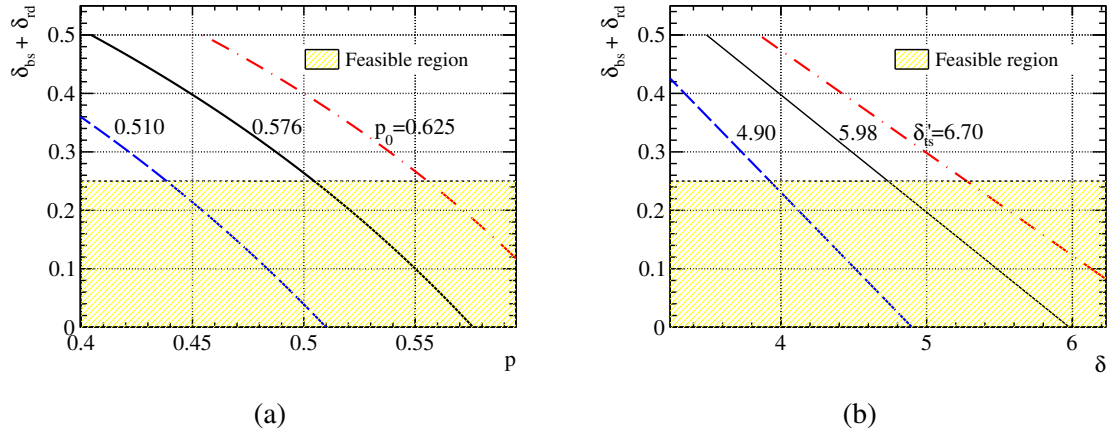

Figure 3.11   Relations of $\delta_{bs} + \delta_{rd}$ against the SEY δ and the fraction of channel mode p. The feasible region shows the consistency of our measurement to the literature.

In Fig. 3.11, with the typical values of $\delta = 5$ and $p = 0.55$, our measurement is consistent with an assumption that $\delta_{bs} + \delta_{rd} < 0.25$. The small contribution of the backscattered and rediffused electrons in SEE is pointed out by Beck[46] to be especially true for insulators with high SEY.

3.1.4 Gamma-Tweedie model for MCP-PMT

In our calculation, the distribution of the MCP charge response to the true-secondary electrons $\Gamma(\alpha_i, \beta_i)$ is determined by their energies E_i, which satisfy $\sum_i^n E_i < E_0$. The incident energy E_0 of the PEs is 650 eV, which is more than ten times the energies of the true secondaries. Because n follows a Poisson distribution with an expectation between 5 and 6.5, the probability of n exceeding 10 is negligible. Thus, the effect of n

on E_i can be ignored, and the energy E_i is independently and identically distributed, as demonstrated in Fig. 3.12(a). The charge response of MCP to a single true-secondary electron, in turn, can be treated identically, as shown in Fig. 3.12(b). Furthermore, a single Gamma distribution $\Gamma(\alpha', \beta')$ is flexible enough to describe the continuous mixture of $\int dE_i \frac{1}{\delta_{ts}} \frac{d\delta_{ts}}{dE_i} \Gamma[\alpha(E_i), \beta(E_i)]$.
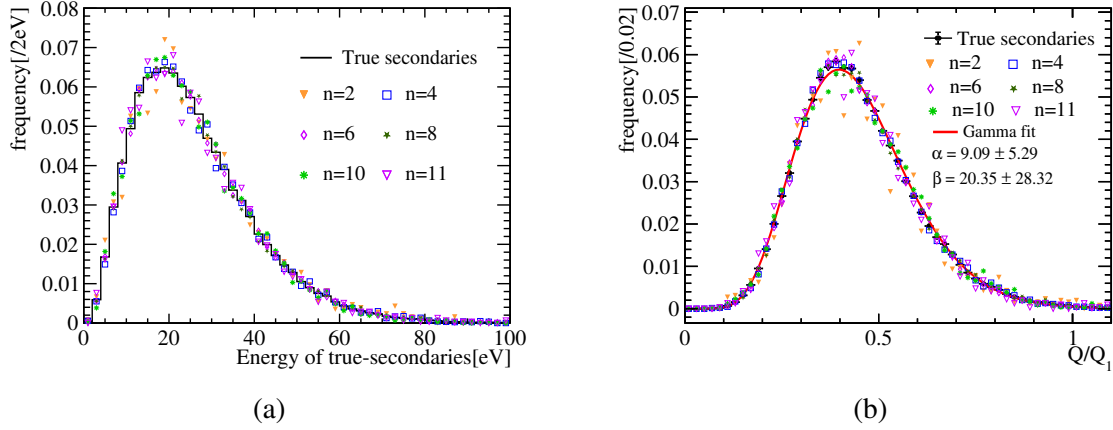

Figure 3.12 The energy distribution and the charge response distribution of MCP to a single true-secondary electron when n is different. (a): All the energies of the true secondaries follow the same distribution, although n is different. (b): the charge response of MCP to a single true-secondary electron is identical, and the fitting of the Gamma distribution $\Gamma(\alpha', \beta')$ achieves sufficient goodness.

When we use such a single $\Gamma(\alpha', \beta')$ in Eq.(3.12), the resulting Poisson-Gamma compound is a special case of the Tweedie distribution $\mathrm{Tw}_\xi(\alpha, \beta)$ for $1 < \xi < 2$[47].

$$
\left.
\begin{array}{l}
Q_{ts} = \sum_{i=1}^{n} Q_i \\
n \sim (\delta'_{ts}) \\
Q_i \sim \Gamma(\alpha', \beta')
\end{array}
\right\} \implies Q_{ts} \sim \mathrm{Tw}_\xi(\alpha', \beta') \tag{3.15}
$$

A phenomenological joint fit of the f_{ch} Gamma and f_{ts} Tweedie mixture with Eq. (3.11) and (3.15) is sufficient to calibrate the SER charge spectrum and measure p_0 and δ'_{ts}. The voltage division experiment (Sec. 3.1.2.3) relations $\mu(E_i)/\sigma(E_i)$ and the Furman model provide the understanding of the jumbo charges and the justification of the phenomenological Gamma-Tweedie mixture, but are less practically useful in PMT calibrations.

The number of parameters, 2 for f_{ch} Gamma and 3 for f_{ts} Tweedie, hinders convergence unless we aid it with physical constraints. Typically $\frac{\alpha'}{\beta'} \approx 0.45Q_1$ and $\sqrt{\frac{\alpha'}{\beta'^2}} \approx 0.15Q_1$. It is practical to bound them in $[0.3, 0.7]Q_1$ and $[0.05, 0.3]Q_1$ when the incident energy E_0 is significantly greater than E_i. We also have checked the chi-square results in the Gamma-Tweedie fitting, which gives good $\chi^2/\mathrm{ndf} < 10$.

In this case, we can write the mathematical model for the SER of the MCP-PMT:

$$f_{\text{MCP-PMT}}(Q) = p_0 \Gamma(Q; \alpha, \beta) + (1 - p_0)\text{Tw}_{\xi}(Q; \alpha', \beta') \tag{3.16}$$

We can get the peak gain $G_p = \alpha/\beta$ and average gain $G_m = p_0\alpha/\beta + (1 - p_0)\delta'_{\text{ts}}\alpha'/\beta'$.

3.2 The timing calibration

3.3 The dark count rate

CHAPTER 4 THE RECONSTRUCTION FOR THE WATER-PHASE

Super-Kamiokande (SK) stands as the world's largest pure water Cherenkov detector, housing 50 kilotons of ultrapure water[48]. Building upon the liquid scintillator-Cherenkov combined track reconstruction technique developed for the MiniBooNE experiment[49], SK collaboration has advanced a likelihood-based reconstruction method, utilizing PMT charge and time information[50], named as fiTQun. For JUNO water-phase, we have implemented targeted improvements to the fiTQun and extended its application to low-energy event reconstruction at the MeV scale.

4.1 The Likelihood function

FiTQun simultaneously determines particle types, vertex positions, momentums, event times. In JUNO water-phase, we just need to determine the vertex position, momentums and event times. The likelihood function of fiTQun is defined as:

$$
\begin{aligned}
\log \mathcal{L}(\boldsymbol{x}; q, t) = & \sum_{j \in \{q=0\}} \log P_j\big(q = 0 \mid \mu_j\big) \\
& + \sum_{i \in \{q>0\}} \log\big(f_{\mathrm{q}}\big(q_i \mid \mu_i\big)\big) \\
& + \sum_{i \in \{q>0\}} \log\big(f_{\mathrm{t}}\big(t_i \mid \boldsymbol{x}\big)\big)
\end{aligned}
\tag{4.1}
$$

- $\boldsymbol{x} = (t_0, x, y, z, p_x, p_y, p_z)$: Event vertex containing time t_0, position (x, y, z), and momentum (p_x, p_y, p_z).
- $\mu_i(\boldsymbol{x})$: Expected PEs at the i-th PMT, computed from the vertex $\boldsymbol{x}$.
- q_i: Charge observed at the i-th PMT, $\{q\}$ is the sequence of q_i, when $q_i = 0$, the PMT is unhitted.
- t_i: Hit time of the i-th PMT, $\{t\}$ is the sequence of t_i.

The first term is the unhit likelihood, which is the probability of no hit in the PMT. The second term is the hit likelihood, which is the probability of detecting hits in the PMT. The third term is the time likelihood, which is the probability of detecting a hit at a certain time.

Since in the operation of the detector, only TQ information (time and charge) is recorded for low-energy events, waveform information is unavailable. At the same time

only the first hit time can be obtained. Therefore, it is necessary to reformulate the likelihood to adopt a first-hit-time-based reconstruction approach. Xuewei Liu et.al developed a first-principles-based reconstruction method using time-charge information or time-PE information in liquid scintillator detectors[51]. We adapt their methodology to reformulate the likelihood function for JUNO water-phase. In low-energy events, where each PMT typically detects only few photon, the number of hits can be directly approximated as NPE (N_{PE}). We can reformulate the likelihood function as Eq. (4.2):

$$
\begin{aligned}
\log \mathcal{L}(\boldsymbol{x}; q, t) = \sum_{j \in \{q=0\}} \log P_j\big(q = 0 \mid \mu_j\big) + \\
\sum_{i \in \{q>0\}} \log\big(f_q\big(0 \mid \mu_{i,T_{low}}^{T_i}\big) * f_t(T_i) * f_q(N_{PE,i} - 1 | \mu_{i,T_i}^{T_{up}})\big)
\end{aligned}
\tag{4.2}
$$

In this case, we define the data taking as $[T_{low}, T_{up}]$, and the first hit time of the i-th PMT as T_i, $\mu_{i,T_{low}}^{T_i}$ is the expected PEs in $[T_{low}, T_i]$, same as $\mu_{i,T_i}^{T_{up}}$.

4.2 Response of the water-phase dector

To compute the likelihood, we need to predict how many photons each PMT will detect when given a vertex. The more accurate the predictions are, the better the reconstruction performances. Therefore, we need a comprehensive understanding of the detector response and develop accurate models for it. It naturally comes to mind that when a charged particle enters water, emits Cherenkov photons, and triggers the PMT, this process can be divided into two parts. One pertains to how Cherenkov light is emitted, while the other concerns how the Cherenkov photons propagate and are detected.

4.2.1 The Cherenkov emission profile

When a charged particle travels through a medium at a speed exceeding that of light, it emits Cherenkov photons within a specific solid angle range. The phenomenon arises from local polarization occurring along the charged particle's trajectory: when polarized molecules return to their ground state, they emit electromagnetic radiation. When the refractive index of the medium is n, and the speed of light in vacuum is c_0, the condition of particle speed v_p for Cherenkov emmision is $\beta = v_p/c_0 > 1/n$. When in pure water, whose refractive index is $n_w = 1.333$, and the paitical is electron ($m_0 = 0.511\,\text{MeV}$), the energy threthold is $E_{th} = m_0 \times (\sqrt{1 - 1/n_w^2} - 1) = 0.262\,\text{MeV}$. That means, only when the energy of electron is larger than $0.262\,\text{MeV}$, the Cherenkov photons will emit.

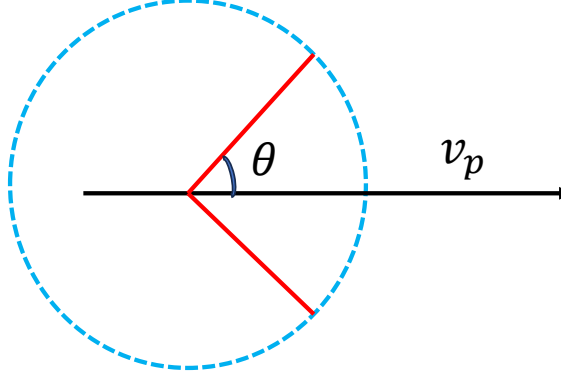The direction of Cherenkov photons can be discribed as: $\cos\theta = \frac{1}{\beta n_w}$ as Fig 4.1 shown.

Figure 4.1　The direction of Cherenkov photons. θ is the angle between the photon emission direction and the direction of particle motion.

When in water, $\cos\theta \approxeq 0.75$. We can use simulation to get the emmision profile of Cherenkov photons. We used JUNO software (version: J24.2.0) for this simulation. Also, we consider the light yield of Cherenkov by simulating electron with momentum from 2 MeV to 30 MeV. Our simulation is based on JUNO software (JUNOsw)[52], and the version is J24.2.1. We simulated electrons with momenta ranging from 2 to 50 MeV, uniformly distributed within the detector, while their emission directions were randomly oriented.

We extended Dou Wei's angular coordinate definition method for liquid scintillator detectors[53] to Cherenkov radiation detection by incorporating momentum direction degrees of freedom, resulting in the coordinate system illustrated in the figure.

In this simulation, we recorded the angles between the emission directions of all Cherenkov photons and the incident direction of the electron, and we do not care the photons are detected or not. Simultaneously, a crucial parameter is the distance between the photon generation point and the origin position of the charged particle.

- From Fig 4.3, most photons are emitted along the Cherenkov angle ($\cos\theta = 0.75$), while a minority exhibit significant angular deviations from the electron's direction. When calculating the emission angle distribution, it must be analyzed separately for different particle energies rather than applying a single angular distribution to electrons of all energies.
- From Fig 4.4, as the particle moves, Cherenkov photons emitted along the initial segment of its trajectory exhibit a uniform distribution. When the particle's velocity
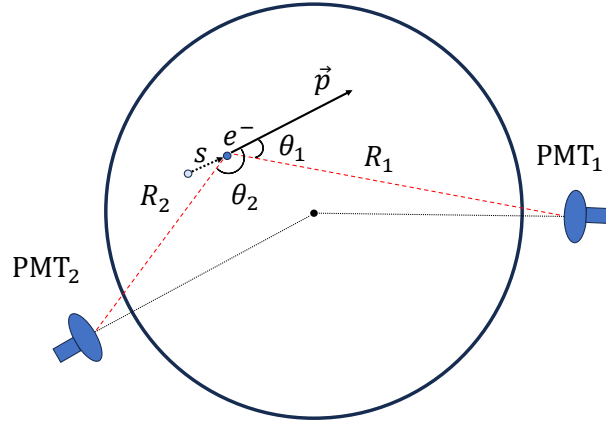
Figure 4.2   Coordinate system definition: θ is the angle of the emission direction of Cherenkov photon and the incident direction of the electron, s is the distance from the position where the particle emits light to its initial position. R is the distance of PMT to the position of electron.

significantly decreases, photon emission drops markedly, with the vast majority of photons being emitted within the first half of the trajectory.
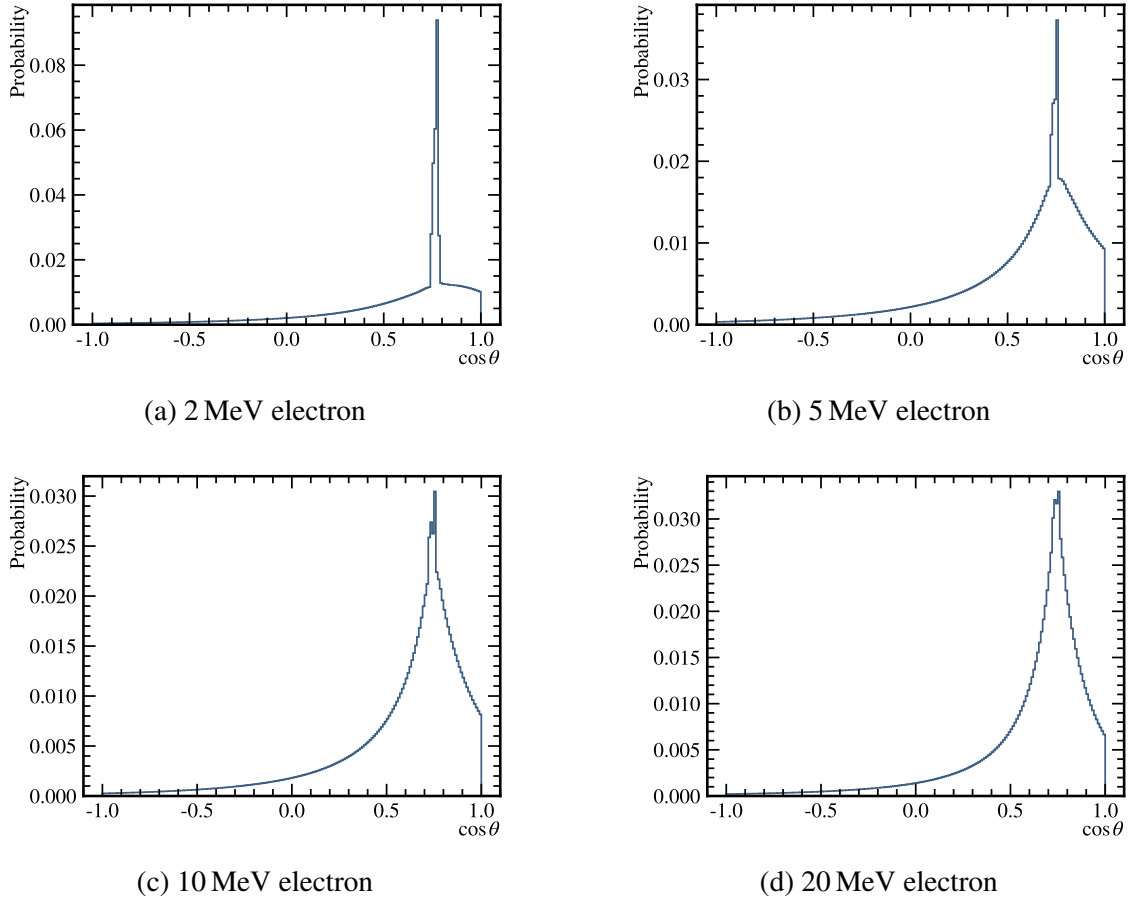
- From Fig 4.5, after traveling some distance, the probability of photons deviating from the Cherenkov angle gradually increases due to multiple scattering. As illustrated in the figure, when electrons undergo multiple scattering, their direction changes significantly, as Fig 4.6 shown. However, when calculating the Cherenkov emission angle, we still use the initial incident direction, thereby producing photons emitted at angles far from the ideal Cherenkov angle.

- In this case, we get the Cherenkov emmision profile ($g(p, s, \theta)$) which describes the proportion of Cherenkov photons emitted at specific locations and directions along the trajectory of a charged particle with a given energy, relative to the total number of emitted photons. For the convenience of research, we use momentum (p) instead of energy (E).

Through Gaussian fitting as shown in Fig 4.7(a) in simulation, we obtain the total number of photons emitted at various energies and calculate the Cherenkov photon yield. After linear fitting, we obtain the relationship between light yield and momentum: $\phi(p) = 1182 \times p - 956$.

4.2.2 The calculation of direct light

After establishing the coordinate system, we can readily determine the number of photons received by a specific PMT when an electron is incident.

$$\mu_{\text{dir}} = \int ds\, g(p, s, \cos\theta)\phi(p)\Omega(R)T(R)\epsilon(\eta) \tag{4.3}$$

(a) 2 MeV electron

(b) 5 MeV electron

(c) 10 MeV electron

(d) 20 MeV electron

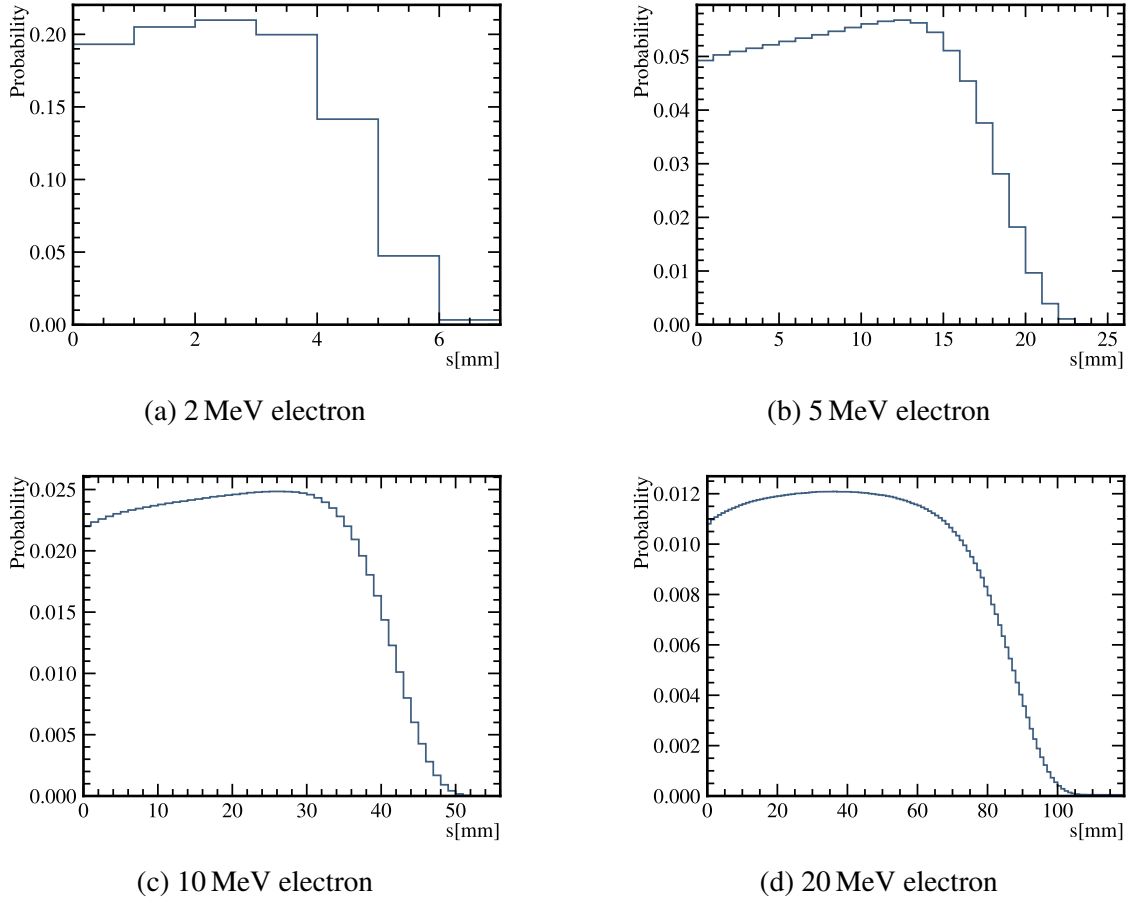Figure 4.3   The relationship of emission probability with $\cos\theta$.

- R is the distance between the position of electron and the PMT.
- $\Omega(R)$ is the solid angle factor of PMT.
- $T(R)$ is the light transmission factor.
- $\epsilon(\eta)$ is the PMT angular acceptance of PMT, and η is the incident angle of light when captured by PMT.

4.2.2.1 The solid angle factor

The main PMTs employed in JUNO are 20-inch with a radius of $a = SI0.622m$. And we can calculate the solid angle of PMT by Eq. (4.4).

$$\Omega(R) = \frac{\pi a^2}{4\pi(R^2 + a^2)} \times (4\pi) = \frac{\pi a^2}{R^2 + a^2} \tag{4.4}$$

This approximation remains valid only when PMTs are sufficiently distant from the particle. In JUNO, PMTs are mounted at around 19.5 m , while our region of interest lies within 17.7 m. Based on SK's experience, the approximation holds effectively at radial distances $R > 1.5$ m.

(a) 2 MeV electron

(b) 5 MeV electron

(c) 10 MeV electron

(d) 20 MeV electron

Figure 4.4   The relationship of emission probability with s.

4.2.2.2 The transmission factor

In our work, we just use Eq. (4.5), and the attenuation length L^a is 75 m.

$$T(R) = \exp(-R/L^a) \tag{4.5}$$

4.2.2.3 PMT angular accptance

4.3 The Fast reconstruction (FRE) of the JUNO water-phase

4.4 The parameters definition

4.4.1 The energy related parameters

For a more accurate description, we define several parameters as follows.

- n_{10}: The maximum count of residual time t_{res} within a 10 ns bin width

- n_b: The average count of t_{res} in [-20, -10] and [30,40]ns.

- n_{20}: The total count of t_{res} in [-20, 20]ns, **primary measure of energy**.

- n_c: The count of $\cos\theta$ in [0.65, 0.85], and the definition of θ is shown in Fig. **??**.

25

(a) 2 MeV electron

(b) 5 MeV electron

(c) 10 MeV electron

(d) 20 MeV electron
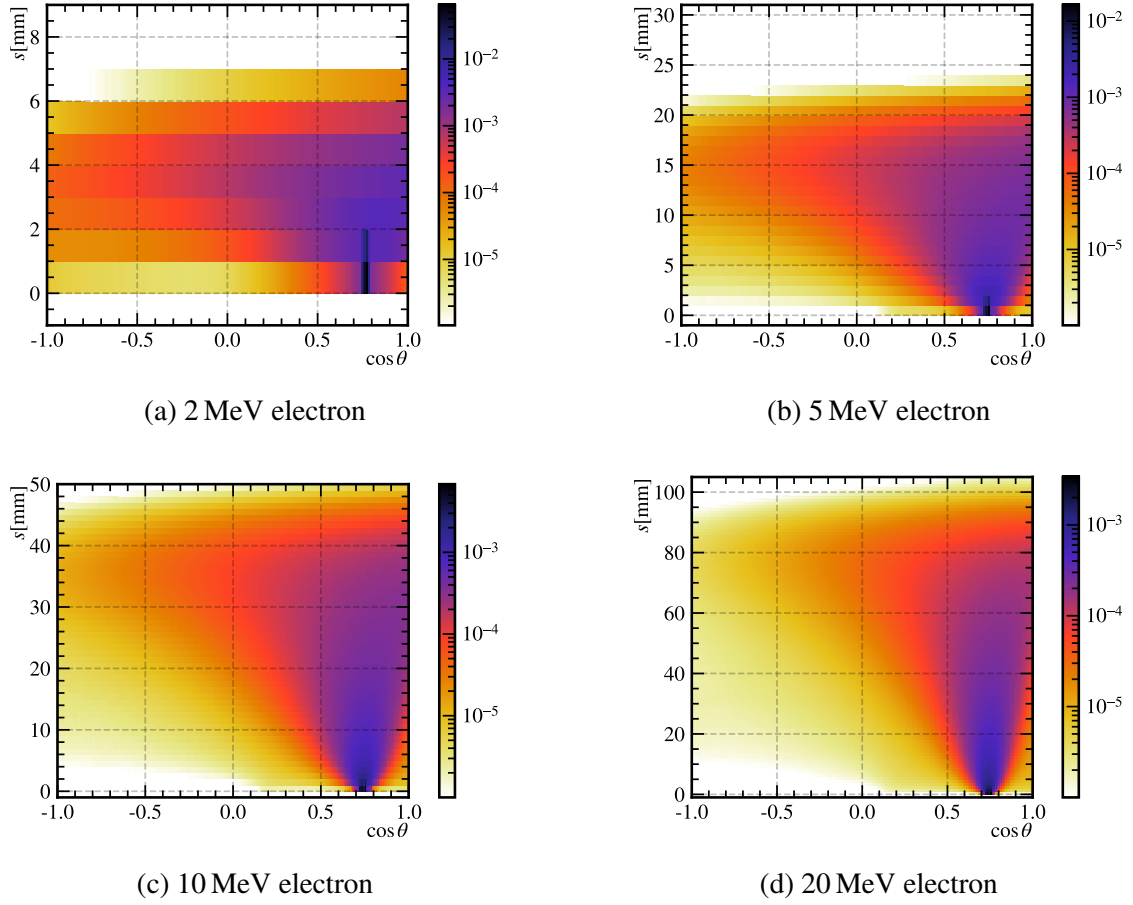
Figure 4.5   The relationship of emission probability with s and $\cos\theta$.

4.4.2 The parameters for reconstruction quality

There exist two types of background, which can exert a significant impact on our analysis. These include the trigger stemming from pure dark noise and the events originating from PMT radioactivity. To eliminate these backgrounds, we introduce several parameters. To comprehensively assess the performance of each parameter, we simulate the uniform distribution of 2.2 MeV Gamma, radioactive events from PMTs, and dark noise trigger events within the detector. Subsequently, reconstruction is performed following the MM trigger.

4.4.2.1 Kurtosis test (k)

The value obtained from the Kurtosis test on the residual time distribution is employed to assess the quality of the signal. In the case where the trigger originates from dark noise, the value should be -1.
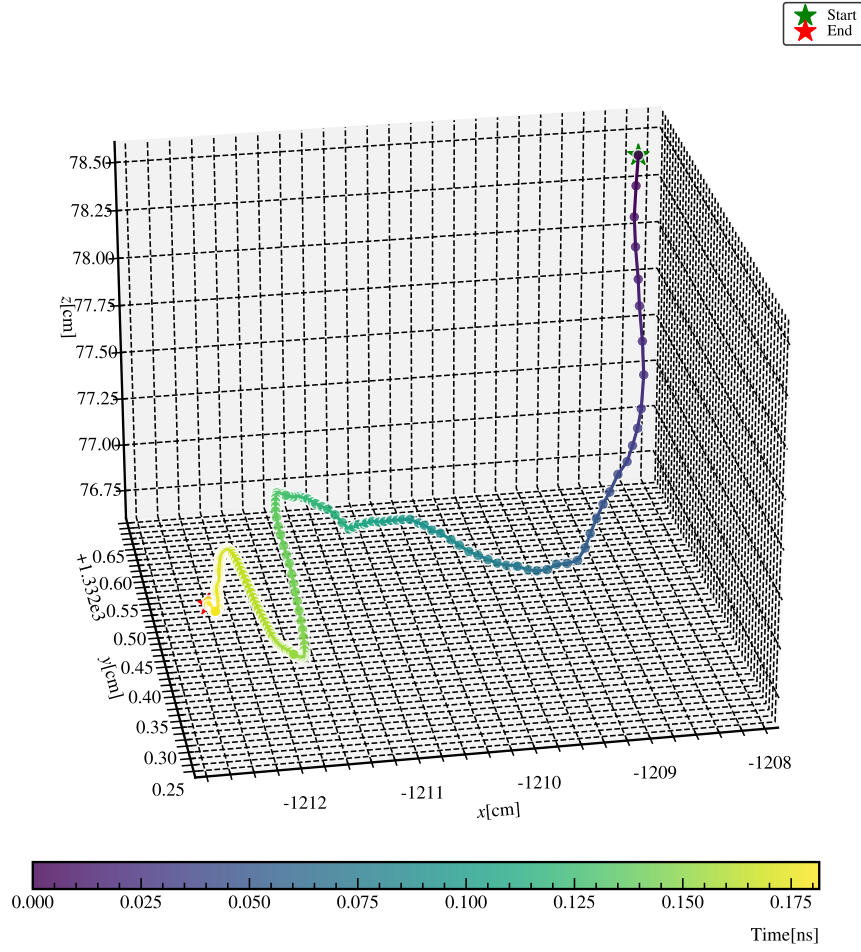
Figure 4.6 An example of a 10 MeV electron undergoing multiple scattering.

4.4.2.2 Akaike Information Criterion (AIC) δA

AIC is frequently employed in model selection. In the context of reconstruction, it is utilized to determine whether the trigger originates from noise or a physical event. This Criterion is defined as Eq. (4.6)

$$\text{AIC}_v = -2\ln\mathcal{L}_v + 2k_p$$
$$\text{AIC}_0 = -2\ln\mathcal{L}_0$$

(4.6)

Where $\mathcal{L}$ represents the likelihood of the event with a single vertex, and k_p denotes the number of reconstructed parameters. During the reconstruction process, we also calculate the likelihood of non-vertex events ($\mathcal{L}_0$). In this scenario, we can obtain the AIC criterion:

$$\delta A = AIC_v - AIC_0 = 14 - 2\ln\mathcal{L}_v + \ln\mathcal{L}_0$$

(4.7)

By comparing δA of dark noise events and 2.2 MeV Gamma events, it can be seen that most dark noise events are eliminated, while less than 10 % of Gamma events are removed.
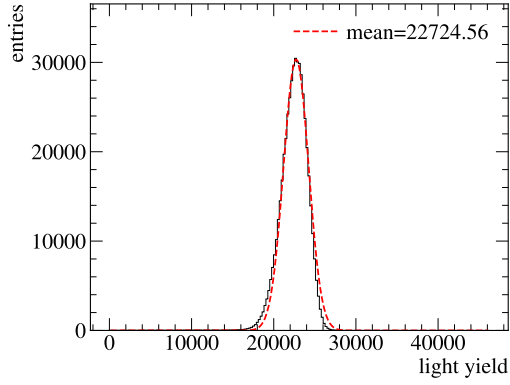
(a) An example of Gaussian fit for light yield.
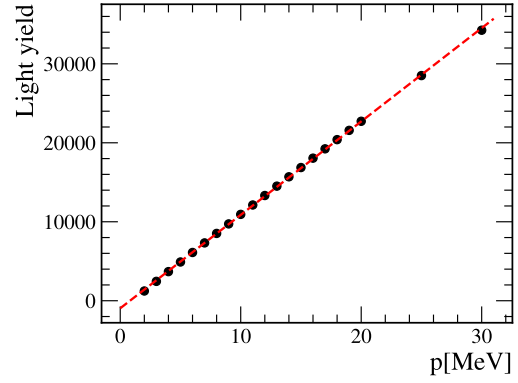
(b) 5 MeV electron

Figure 4.7　The relationship of emission probability with s and .
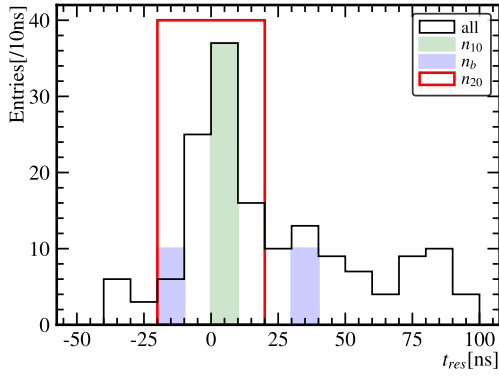
(a) The distribution of t_{res}.
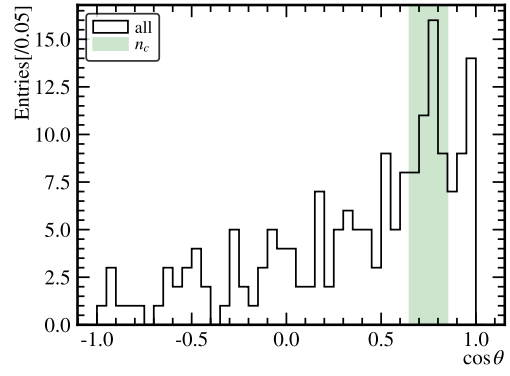
(b) The distribution of $\cos\theta$.

Figure 4.8　The definition of parameters related to energy.

4.4.2.3 The likelihood-energy combined Criterion (LE)

We define the likelihood-energy combined criterion as LE, as Eq. (4.8)

$$LE = -\ln\mathcal{L}/n_{20} \tag{4.8}$$

This criterion is employed to eliminate events stemming from PMT radioactivity. When the cut $LE < 40$ is applied, over 99.99 % of the events from PMT radioactivity are removed, along with approximately 30 % of the 2.2 MeV Gamma.

4.4.2.4 The goodness of reconstruction (G_{vd})

When contemplating reconstruction, it is essential to assess the quality of both position and direction. In the case of a successfully reconstructed position, the residual time should be distributed as closely as feasible around zero. For precise direction reconstruction, PMTs adjacent to the Cherenkov ring ought to demonstrate uniform photon acceptance. In accordance with these criteria, we formulate the following two goodness
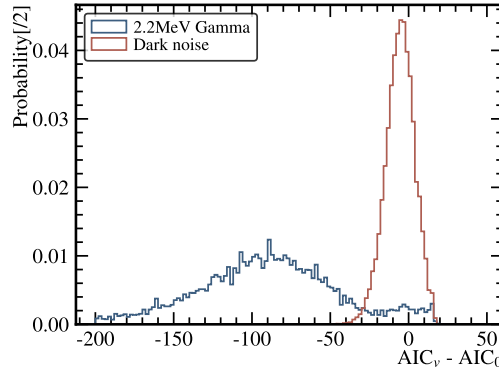
Figure 4.9   There is obvious difference between dark noise and 2.2 MeV Gamma. We can optimize it to remove dark noise events.
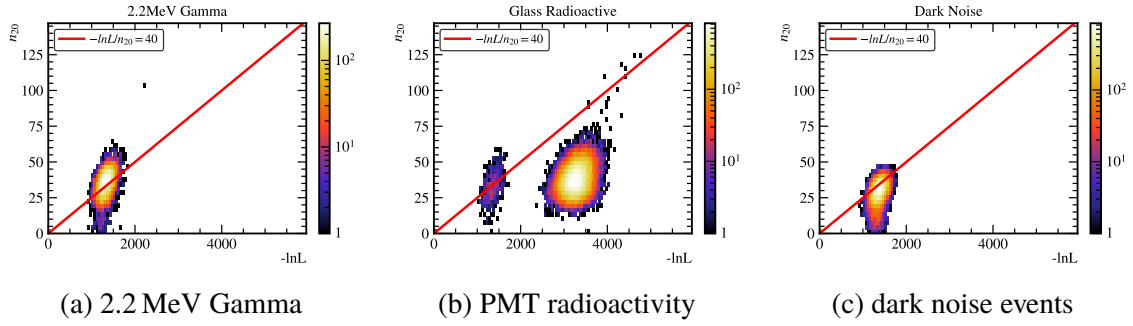

(a) 2.2 MeV Gamma   (b) PMT radioactivity   (c) dark noise events

Figure 4.10   The relationship between $\mathcal{L}$ and n_{20}.

metrics, presented as Eq. (4.9). Finally, we combine these two metrics to obtain the overall goodness of reconstruction, denoted as $G_{vd} = g_v^2 - g_d^2$.

$$g_v = \frac{\sum e^{-0.5(t_{res}/w)^2} e^{-0.5(t_{res}/\sigma)^2}}{\sum e^{-0.5(t_{res}/w)^2}}$$
$$g_d = \frac{1}{2\pi} \left[\max\left(\phi_i - \frac{2i\pi}{N} \right) - \min\left(\phi_i - \frac{2i\pi}{N} \right) \right]$$

(4.9)

- w and σ: in this work, $w = 20$ ns and σ is the TTS of PMT.

- g_v: The goodness of position reconstruction.

- g_d: The goodness of direction, describes the uniformity of the azimuthal angle distribution, as shown in Fig. 4.11.

4.4.3 In the dector simulation
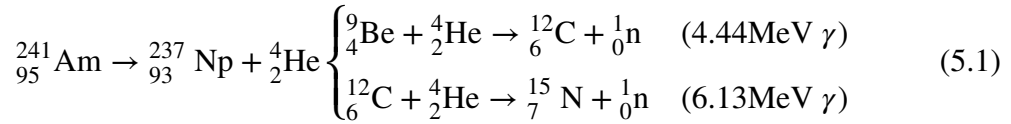
4.4.4 In the electronic simulation
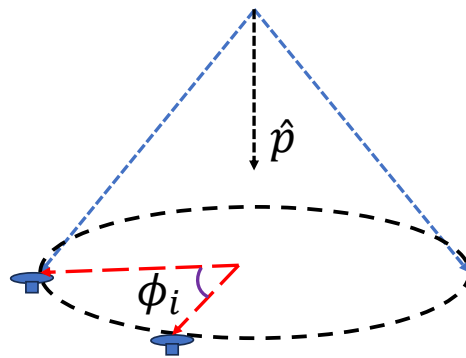
Figure 4.11 The definition of azimuthal angle in the goodness of direction calculation.

CHAPTER 5 NEUTRON DETECTION IN JUNO WATER PHASE

5.1 JUNO's low-energy threshold in water phase

5.1.1 The source calibration in water phase

Americium-Beryllium (AmBe) and Americium-Carbon (AmC) neutron sources serve as critical reference standards for characterizing neutron detecting capabilities. Both sources leverage the alpha decay of ^{241}Am. The neutron producing process can be described as Eq. (5.1):

$$^{241}_{95}\text{Am} \rightarrow {}^{237}_{93}\text{Np} + {}^{4}_{2}\text{He} \begin{cases} {}^{9}_{4}\text{Be} + {}^{4}_{2}\text{He} \rightarrow {}^{12}_{6}\text{C} + {}^{1}_{0}\text{n} & (4.44\text{MeV } \gamma) \\ {}^{12}_{6}\text{C} + {}^{4}_{2}\text{He} \rightarrow {}^{15}_{7}\text{N} + {}^{1}_{0}\text{n} & (6.13\text{MeV } \gamma) \end{cases} \qquad (5.1)$$

During the water phase, neutron source calibration was performed three times, and the summary of 14 runs are in Table. 5.1. All the calibration sources were placed along

Table 5.1 **The neutron source calibration in water phase**

Calibration	Date	Configuration
First	02/02	AmC, threshold=53, Run 3279, 3281, 3283, 3286, 3293
Second	02/03	AmBe, threshold=53, Run 3333, 3335, 3338, 3340, 3342
Final	02/07	AmBe, threshold=46.5, Run 3660, 3663, 3671; AmC, threshold=44, Run 3675

the z-axis, as Fig. 5.1 shown. To enhance our capability in studying low-energy events in water phase, we decouple and analyze prompt and delayed signals separately during the calibration source analysis.

5.1.2 The reconstruction of the prompt signals

5.1.2.1 The event selection before reconstruction

In this study, we take Run 3671 (calibrated with a AmBe source at the position of $(0, 0, -10\,\text{m})$) as an illustrative example. To mitigate the data volume, we selectively choose a subset of events from the previous findings (JUNO-doc-12539) based on Baona's reconstruction method. Additionally, partial background events are filtered out. After
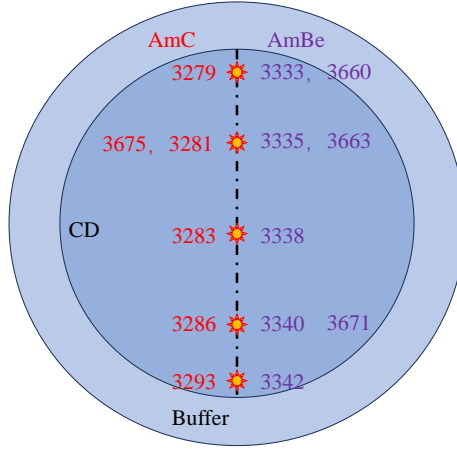
Figure 5.1   The calibration source positions in water phase.

applying a fiducial volume of 17 m cut, we observed that a large number of events were downward, as depicted in Fig. 5.2.
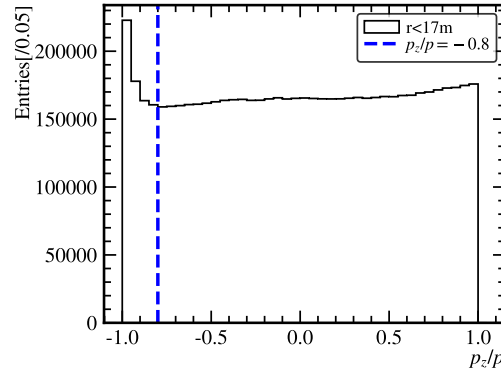

Figure 5.2   The distribution of p_z/p after applying a fiducial volume of 17 m cut.

We require additional directional cuts. Therefore, our selection criteria are as follows.

• Fiducial volume $r < 17$ m

• isglass < 0.5

• score > 0.001

• $p_z/p > -0.8$

• $n_{20} > 12$

To demonstrate the events selection during the cut process, we apply a cylindrical cut with a radius of 2 m along the z-axis and plot the z-coordinate distribution of events as shown in Fig. 5.3.

After event selection, additional constraints are applied to the PMT photoelectron (PE) timing distribution. The PE times are binned with a width of 48 ns over the interval $t \in [96, 576]$ns. A 180 ns reconstruction window is then defined, comprising 36 ns before

32
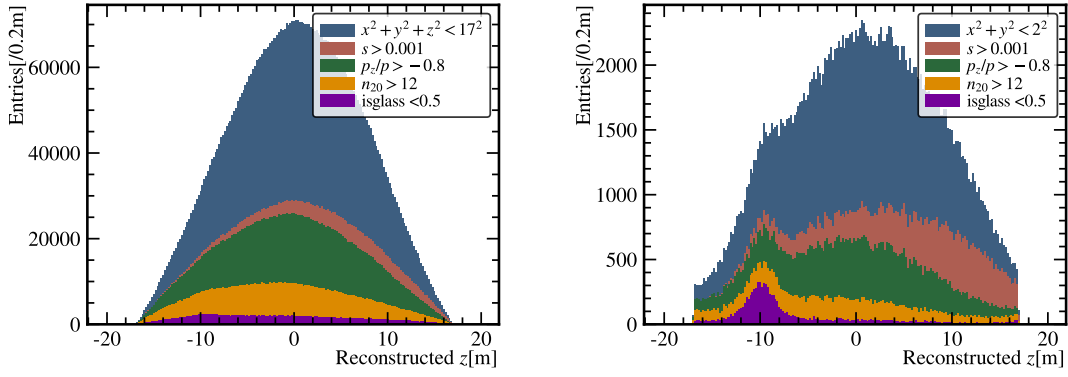
Figure 5.3   The distribution of z-coordinate in Run 3671. () shows the distribution without cylindrical cut, while () shows the distribution after the cut.

and 144 ns after the maximum bin within the search range, as illustrated in Fig. 5.4. This selection effectively suppresses dark noise contributions and improves the robustness of the vertex reconstruction.
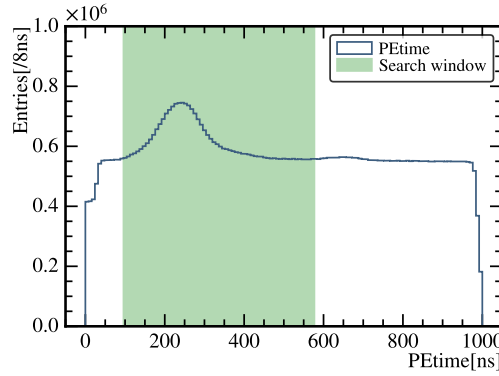

Figure 5.4   The PE time distribution in Run 3671. We search the maximum bin in the green range and select a 180 ns time window for reconstruction.

5.1.2.2 The position distribution of the prompt signals

The prompt signal reconstruction employs the maximum likelihood method described in Sec. 4.1. Subsequently, quality and background rejection cuts are applied to remove events with poor reconstruction performance and residual background contamination. The specific cuts are as follows:

- Fiducial volume: $r < 16.5$m
- Unknown downwards events: $p_z/p > -0.8$
- Signal quality: $k > -0.85$
- Energy related: $n_{10} - n_b > 15$ and $n_c > 8$

After these selection cuts, pronounced event clustering is visible near the calibration
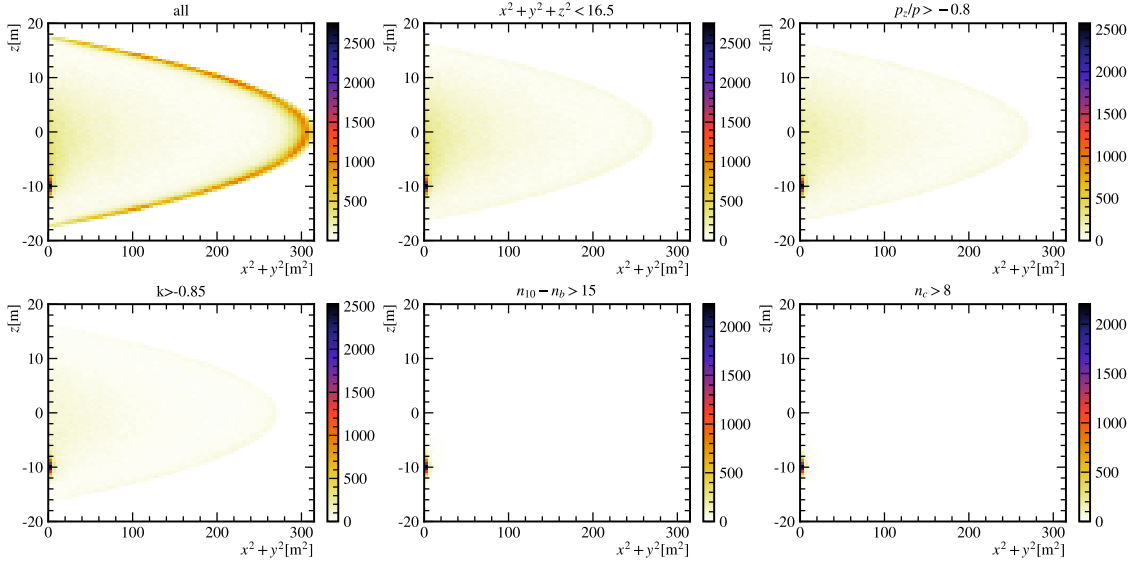
Figure 5.5   The position distribution of the prompt signals in Run 3671.

source position. Furthermore, applying a $2\,\mathrm{m}$ cylindrical cut along the z-axis yields a prominent peak at $z = -10\,\mathrm{m}$ in the reconstructed event distribution, as shown in Fig. 5.6.
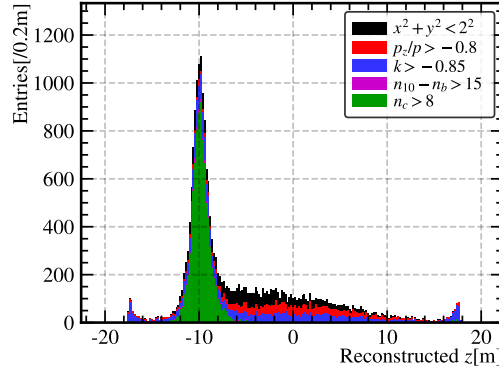

Figure 5.6   The distribution of z-coordinate in Run 3671 after $2\,\mathrm{m}$ cylindrical cut.

Applying the same selection cuts and analysis procedure, the reconstructed vertex position distributions of prompt signals are obtained for 14 calibration runs. As shown in Fig. 5.7, prompt signals from both AmC and AmBe sources are accurately reconstructed at their deployment positions, validating the performance of the position reconstruction algorithm. These results further demonstrate that JUNO's water phase is capable of detecting $6.1\,\mathrm{MeV}$ and $4.4\,\mathrm{MeV}$ Gamma signals with high statistical significance.
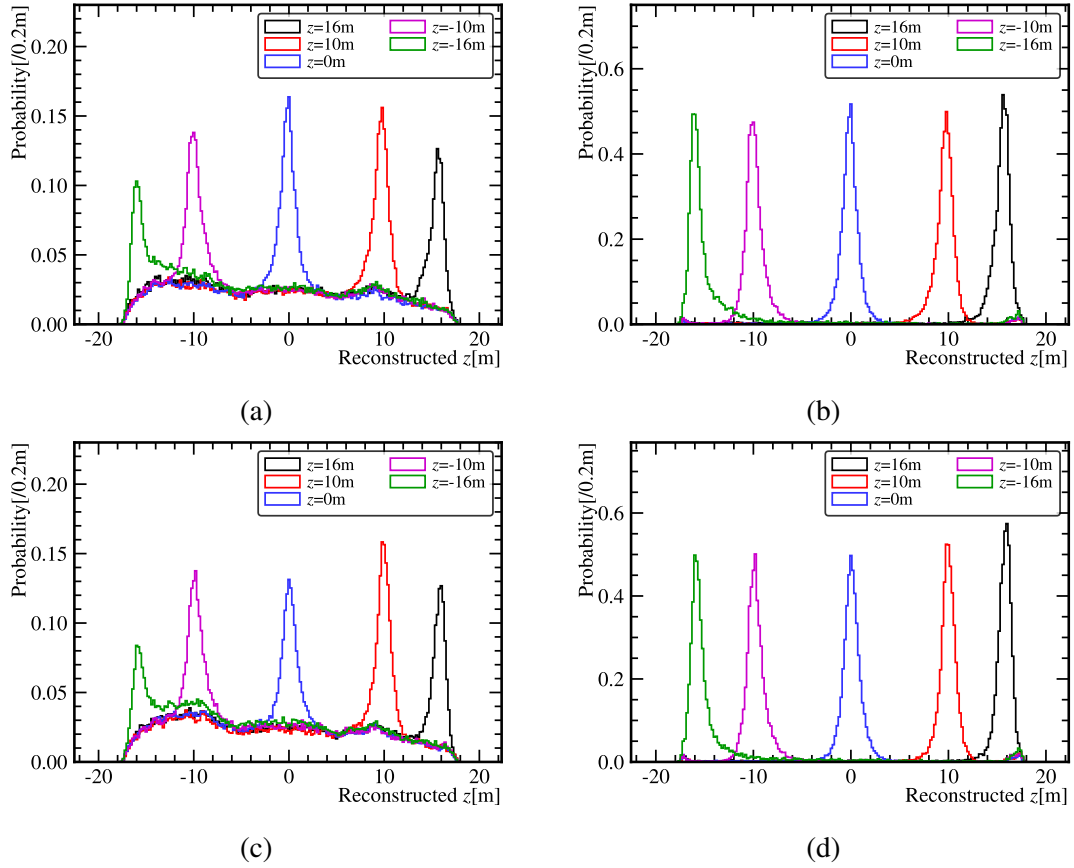
(a)

(b)

(c)

(d)

Figure 5.7 The distribution of z-coordinate in AmC and AmBe source calibration. ((a)) and ((c)) show the distribution without cylindrical cut, while ((b)) and ((d)) show the distribution after the cut of 2 m cylinder along the z-axis. ((a)) and ((b)) are the results of AmC source calibration, and ((c)) and ((d)) are the results of AmBe source calibration respectively.

5.1.2.3 The energy distribution of prompt signals

To obtain the energy spectrum of the prompt signals, all events within a 3 m radius of the calibration source position are selected, as shown in Fig. 5.8. To account for the influ-
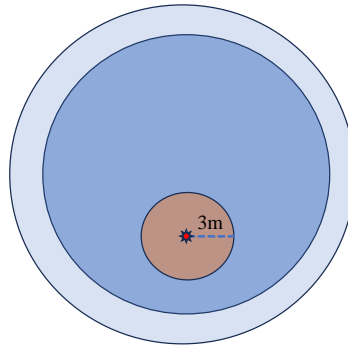
Figure 5.8   3-meter radius cut around the calibration source position

ence of the background energy distribution, data collected under identical conditions but without a calibration source at the same location are used. For Run 3671, the background

spectrum is derived from Run 3663. To mitigate the impact of differing data acquisition durations, the energy spectra are normalized to live time, allowing event rates to serve as the primary comparison metric. As shown in Fig. 5.9(a), substantial background contamination remains in the energy spectrum despite the application of selection cuts. After background subtraction, the n_{20} distribution for 4.4 MeV Gamma events is obtained. Similarly, for Run 3286, which utilizes an AmC source, the background spectrum is derived from Run 3281. The n_{20} distribution for 6.1 MeV Gamma events is shown in Fig. 5.9(b).

| (a) | (b) |
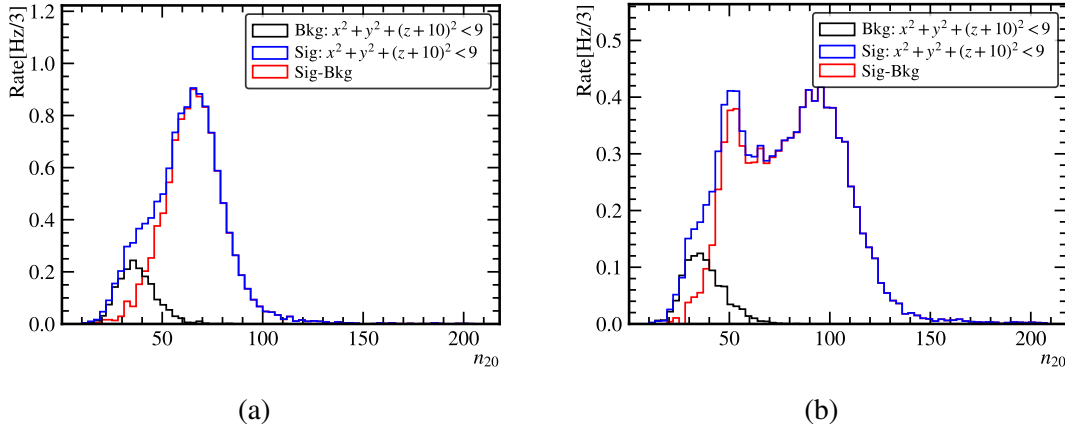
Figure 5.9   The energy distribution of prompt signals. The black line represents the background energy distribution, the blue line represents the energy distribution of prompt signals, and the red line represents the prompt signal energy distribution after subtracting the background. ((a)) is the result of Run 3671, representing the energy distribution of 4.4 MeV Gamma. ((b)) is the result of Run 3286, representing the energy distribution of 6.1 MeV Gamma.

5.1.3 The search for delayed signals

5.1.3.1 The reconstruction of delayed signals

After applying the aforementioned selection criteria, prompt signal candidates are identified. We then investigate the delayed signals arising from neutron capture events. To reconstruct these delayed signals while reducing data volume, a coincidence reconstruction algorithm is employed. As shown in Fig. 5.10, a 1000 us time window is used for delayed signal reconstruction. For the study of accidental coincidence backgrounds, additional events are reconstructed within the 1000–2000 us interval.

5.1.3.2 The search for delayed signals

After the delayed signal reconstruction, we apply the following criteria to select delayed signals:

- The selection of prompt signals:

"prompt"
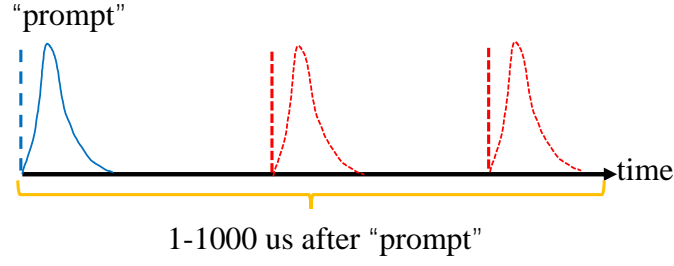
time

1-1000 us after "prompt"

Figure 5.10　The delayed signal reconstruction time window.

- Energy related cut: $n_{10} - n_b > 15$.
- Directional cut: $p_z/p > -0.8$.
- Distance to the source: < 3 m.
- Muon veto: > 500 us.
- Background cut: $\delta A < -50$, $LE < 40$.

• The selection of delayed signals:

- Energy related cut: $32 < n_{20} - n_b < 70$.
- Coincident distance $dR < 6$ m.
- Directional cut: $p_z/p > -0.8$.
- muon veto: > 500 us.
- Coincident time: $dT < 1000$ us.
- Background cut: $\delta A < -50$, $LE < 40$.

Following the series of selection procedures, an exponential fit,

$$f(t) = A \exp(-t/\tau) + c \tag{5.2}$$

is performed on the coincidence time distribution between prompt and delayed signals, as shown in Fig. 5.11. The extracted neutron capture lifetime is 203 ± 24 us, in agreement with theoretical expectations within experimental uncertainties. In parallel, the position distributions of both prompt and delayed signals are examined. As illustrated in Fig. 5.12, events are strongly clustered around the calibration source location, consistent with the deployment geometry. These results demonstrate that the JUNO detector exhibits robust neutron detection capability during the water phase.

5.1.4 The low-energy threshold in water phase

Through a detailed analysis of calibration source data, distinct Gamma signals at 6.1 MeV and 4.4 MeV are identified, in addition to the characteristic 2.2 MeV Gamma signal originating from neutron capture on hydrogen. To obtain a cleaner prompt signal
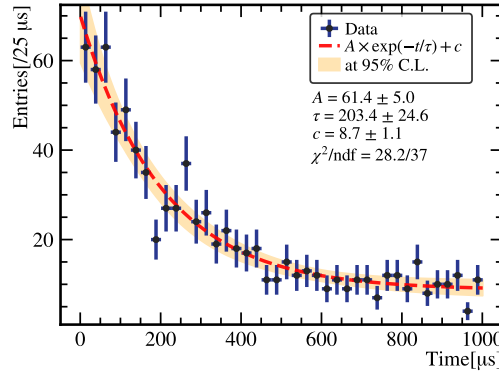
Figure 5.11 The coincident time fit.

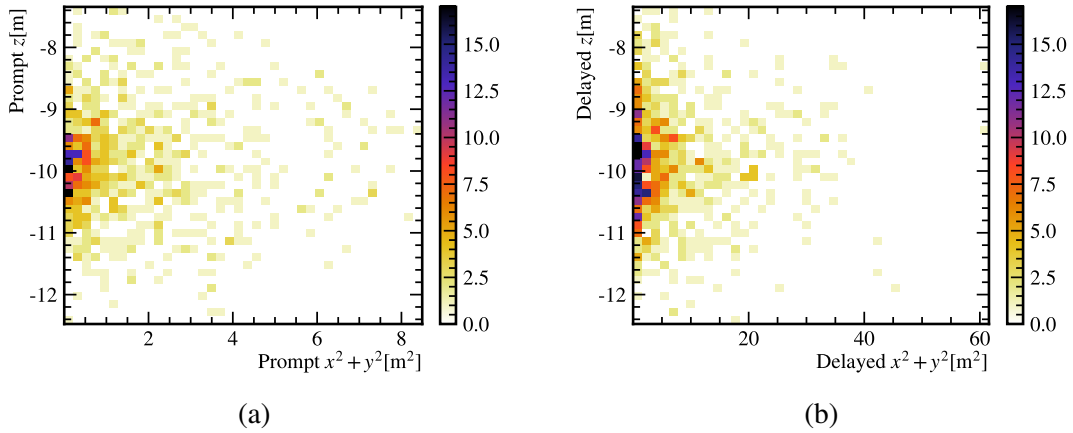(a)   (b)

Figure 5.12 The position distribution of prompt and delayed signals. ((a)) is the position distribution of prompt signals, and ((b)) is the position distribution of delayed signals.

energy spectrum, additional selection criteria are applied beyond the initial cuts. Specifically, prompt events are required to satisfy $\delta A < -50$, and, for the AmC source, the condition $n_{10} - n_b > 20$ is imposed. These requirements enhance the purity of the prompt signal spectrum. The energy spectrum of the 4.4 MeV Gamma is shown in Fig. 5.13(a), while that of the 6.1 MeV Gamma is shown in Fig. 5.13(b). Furthermore, the energy cut used in the coincidence analysis is removed. Coincidences occurring within 1000 us are designated as signal, while those in the 1000–2000 us window are taken as background. Using this approach, the energy distribution of the 2.2 MeV Gamma from neutron capture on hydrogen is obtained, as shown in Fig. 5.13(c).

After obtaining the energy spectra of the three characteristic signals, we perform Gaussian fitting to quantify their spectral parameters, as shown in Fig. 5.14. When we use n_{20} to estimate the energy, the light yield is 14.0 ± 0.1 PE/MeV. Simultaneously, we estimate that each triggered physical event contains an average of 8.1 PE originating from PMT dark noise and so on.
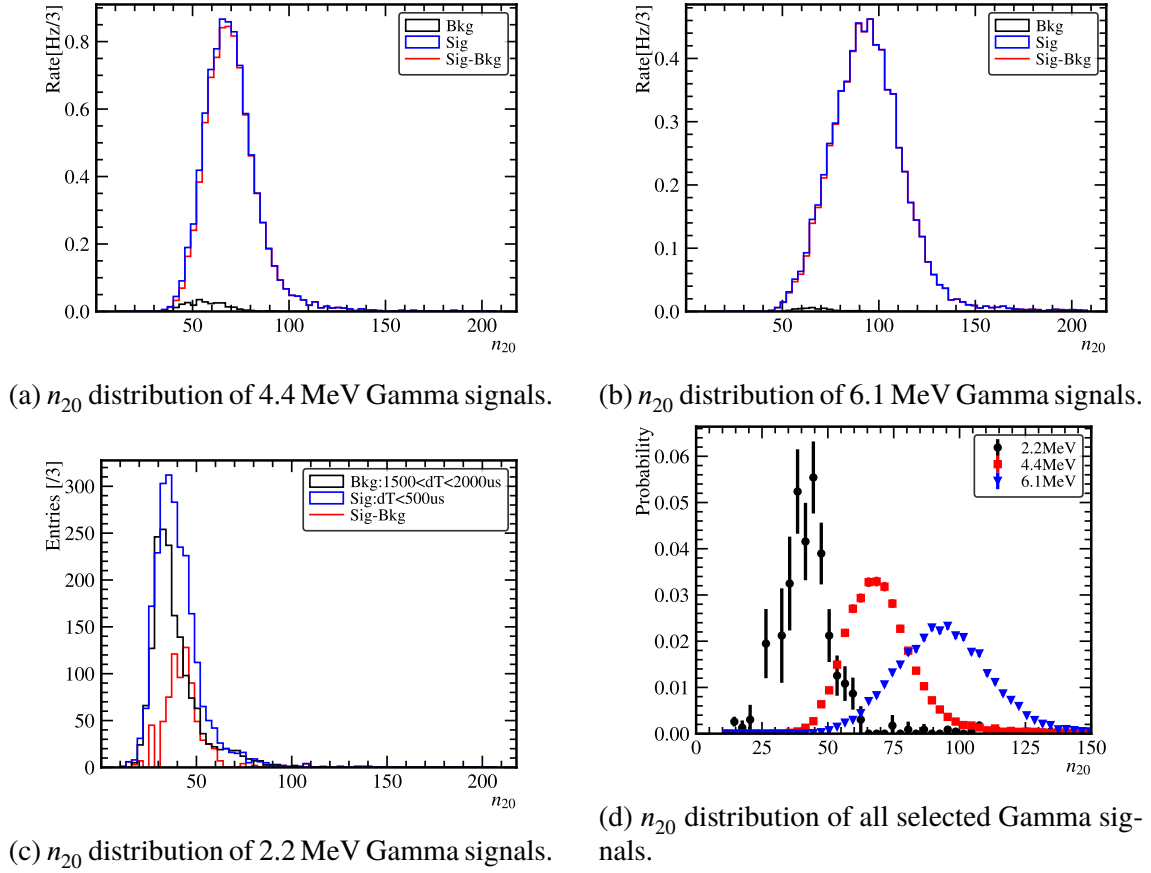
(a) n_{20} distribution of 4.4 MeV Gamma signals.

(b) n_{20} distribution of 6.1 MeV Gamma signals.

(c) n_{20} distribution of 2.2 MeV Gamma signals.

(d) n_{20} distribution of all selected Gamma signals.

Figure 5.13   The n_{20} distributions for 2.2 MeV, 4.4 MeV, and 6.1 MeV Gamma signals, as well as the combined spectrum of all selected Gamma events.

5.2 The neutron capture detecting ability of JUNO in water phase

Neutron detection efficiency and SNR are critical parameters in the design and optimization of neutron detection systems, as it directly determines the accuracy and sensitivity of experimental measurements. In this section, we will discuss the neutron detection efficiency and SNR of the JUNO detector in the water. In Sec. 5.1.3.2, the delayed signals were successfully reconstructed, and the neutron capture on hydrogen lifetime was obtained. However, the efficiency of n-H capture tagging has yet to be determined. To evaluate this, the prompt candidates are analyzed to calculate the n-H capture tagging efficiency. After prompt signal reconstruction and selection, a total of N_p prompt candidates are obtained, and the corresponding background contribution, N_{pb}, is estimated from dedicated background runs. Among these prompt candidates, N_0 delayed candidates satisfy the n-H capture selection criteria. Following a lifetime fit in which the coincidence time is binned into N_b intervals, as illustrated in Fig. 5.11, the number of accidental coincidence pairs is estimated as $c \times N_b$. Thus, the net number of n-H capture events is calculated as $N_{\mathrm{nH}} = N_0 - c \times N_b$. The tagging efficiency (η) and the signal-to-noise ratio (SNR) are
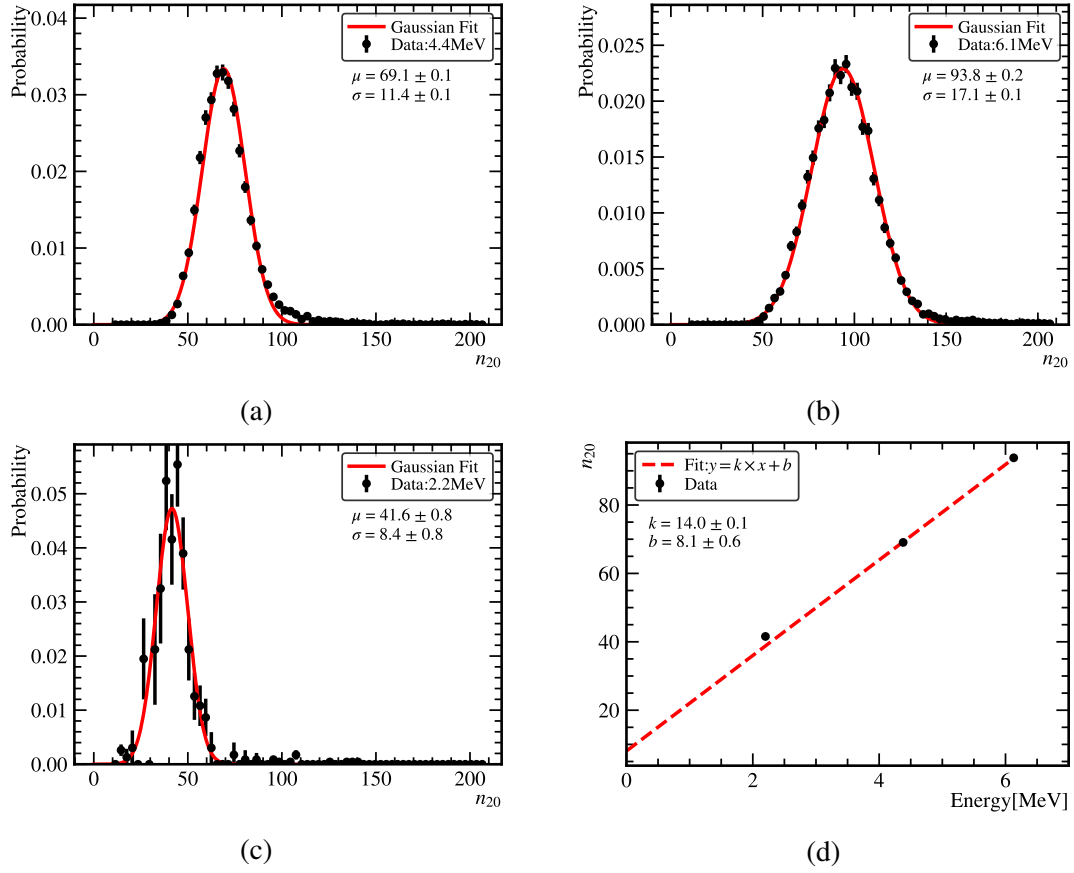
39

Figure 5.14   Gaussian fit of the n_{20} distribution of 4.4, 6.1 and 2.2 MeV Gamma signals. ((d)) is the Cherenkov light yiled fit.

defined in Eq. (5.3).

$$\eta = (N_0 - c \cdot N_b)/(N_p - N_{pb})$$
$$\text{SNR} = (N_0 - c \cdot N_b)/\sqrt{c \cdot N_b}$$

(5.3)

As discussed in Sec. 4.1, the application of background suppression techniques inevitably leads to a partial loss of delayed neutron capture events. To evaluate the detector performance, a comprehensive parameter scan was conducted over an extended operational parameter space. This systematic study aims to determine both the maximum attainable neutron detection efficiency and SNR for neutron tagging. The parameters scanned for neutron tagging are summarized in Table 5.2. Following event selection, an n-H capture lifetime fit is performed. The fitted lifetime is required to satisfy the following criteria:

- Fitted lifetime falls within the range of 185–230 us. For calibration runs at $z = -16$ m: 3293 and 3342, the neutron capture lifetime constraint has been relaxed to the range of 170–250 us, while at $z = 16$ m: 3279 and 3333, the constraint remains at 180–230 us, as evidenced in Fig. 5.15.

- Contain the reference value of 207 us within its 1σ uncertainty interval.

Table 5.2 **Neutron Tagging Optimization Parameter Scan Specifications**

Parameters	Range	Step or Point
Coincident distance (dR,m)	3–12	1
Energy related (n_{20})	0–49	2 when $9 < n_{20} < 25$; 1 when $25 < n_{20} < 50$
AIC criteria (δA)	-70–0	5
LE criteria (LE)	36–200	200, 150, 100, 50, 45, 43, 42, 41, 40, 39, 38 ,36
Goodness (G_{vd})	-0.1–0.15	0.02 when $G_{vd} < 0$; 0.01 when $G_{vd} > 0$
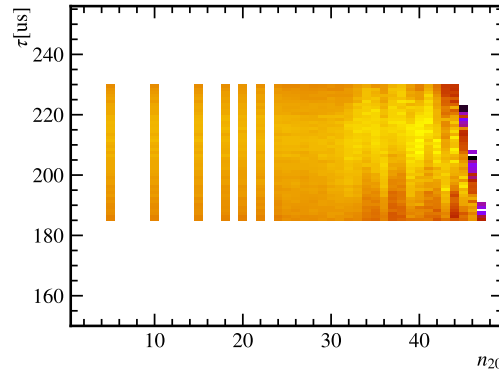
Figure 5.15   The fitted lifetime of Run 3671.

Simultaneously, we examine the χ^2/ndf values of all fits, which consistently fall near 1.0, indicating excellent fit quality across the analyses, as shown in Fig. 5.16.
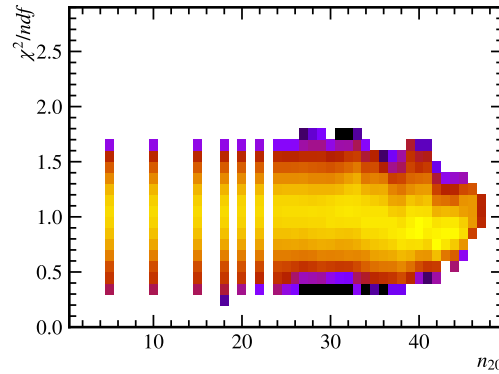
Figure 5.16 χ^2/ndf values changes with the n_{20}, but still around 1.0.

5.2.1 The maximum neutron detection efficiency

Maximizing neutron detection efficiency is crucial for capturing the largest possible fraction of neutron capture events, thereby improving statistical precision and extending the sensitivity of the detector to rare processes. In this context, the parameter scan results are examined to identify the configuration yielding the highest efficiency within the

allowed lifetime selection criteria. As illustrated in Fig. 5.17, the maximum neutron detection efficiency achieved is 10 % in Run 3671, with the corresponding selection parameters as shown in Table 5.3.

Table 5.3 **The parameters when get the highest efficiency**

Parameters	Selection
Coincident distance (dR,m)	< 11 m
Energy related (n_{20})	> 27
AIC criteria (δA)	< −5
LE criteria (LE)	< 200
Goodness (G_{vd})	> 0.02

As shown in Fig. 5.18, we select the highest-efficiency events in Run 3671. The position distributions of the prompt and delayed signals are presented in Figs. 5.18(a) and 5.18(b), respectively. The prompt-signal distribution is consistent with the position of the deployed calibration source, while the delayed signals are observed to cluster around the corresponding prompt vertices. This position correlation indicates that the delayed signals originate predominantly from neutron captures on hydrogen, as expected. As illustrated in Fig. 5.19, the fitted neutron-capture lifetime is measured to be 207.2 ± 47.2 us, in agreement with the theoretical expectation. The resulting fit yields a χ^2/ndf of 27.3/30, demonstrating good fit quality.
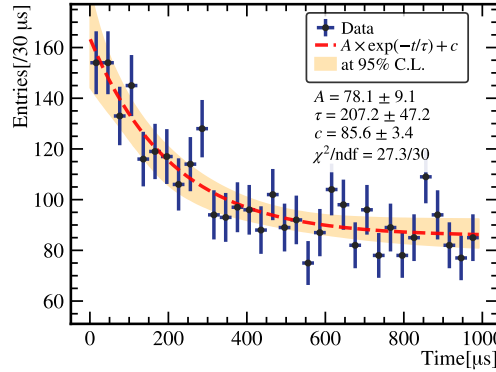

Figure 5.19   The lifetime fit when getting the highest efficiency events in Run 3671.

As illustrated in Fig. 5.20, neutron detection efficiency exceeding 10 % has been experimentally achieved, as validated through comprehensive calibration campaigns with AmBe and AmC neutron sources. During the calibrations on February 2-nd, the higher MM-trigger threshold resulted in an overall lower neutron detection efficiency compared

(a) Efficiency vs. dR

(b) Efficiency vs. n_{20}

(c) Efficiency vs. δA

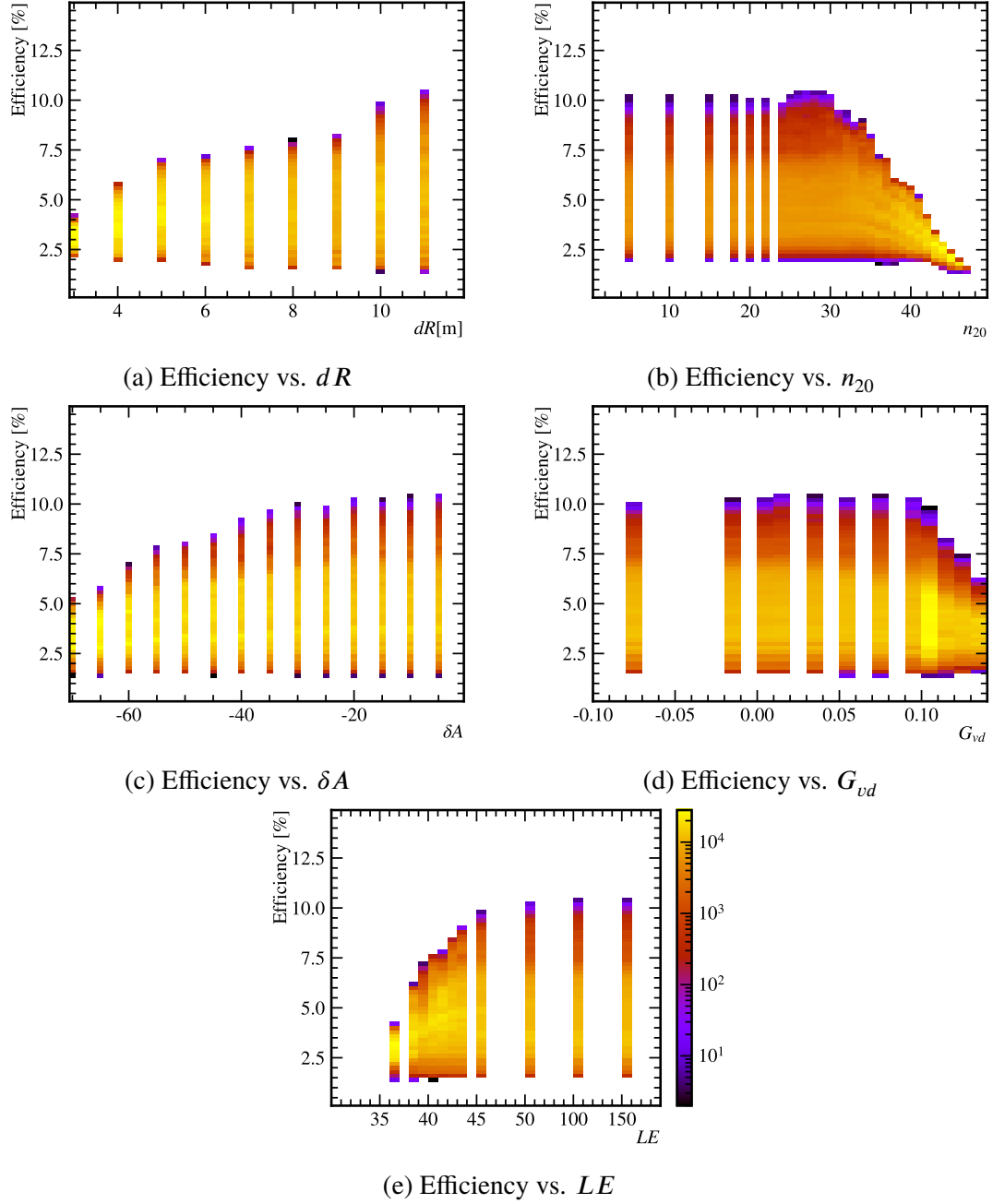(d) Efficiency vs. G_{vd}

(e) Efficiency vs. LE

Figure 5.17   Neutron detection efficiency as a function of five key selection parameters in Run 3671. The maximum efficiency achieved is 11.7 %.
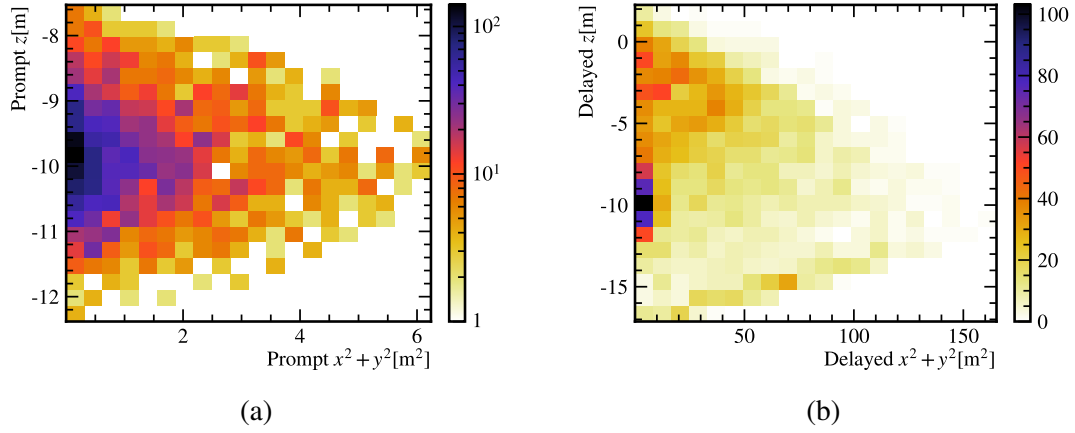
Figure 5.18 The position distribution when getting the highest efficiency in Run 3671. ((a)) is the position distribution of the prompt signals, and ((b)) is of the delayed signals.

to results of calibrations on February 2-nd. Simultaneously, significant asymmetry is observed between the positive and negative z-axis regions: detection efficiency in the negative z-axis is notably lower than in the positive z-axis, with the most pronounced deficit occurring at the 16 m position. This demonstrates clear non-uniformity in JUNO's detector performance during the water phase.
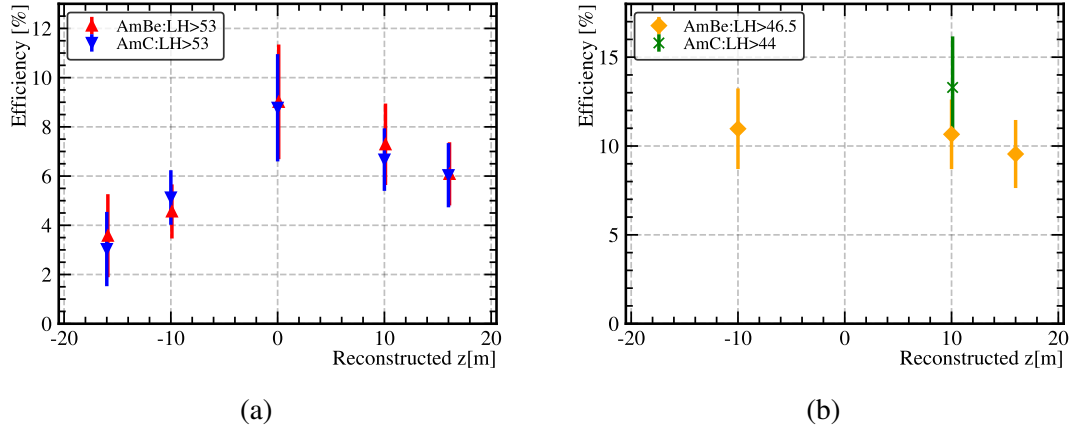
Figure 5.20 The final highest neutron detection efficiency in all 14 calibration runs. ((a)) is the result of calibrations on February 2-nd, and ((b)) is of calibrations on February 7-th.

5.2.2 The highest neutron detection signal-to-noise ratio

Maximizing the signal-to-noise ratio (SNR) is essential for enhancing the clarity of true signal events relative to background fluctuations, thereby improving measurement accuracy and extending the detector's capability to resolve subtle physical effects. In this context, the parameter scan results are analyzed to identify the configuration yielding the highest SNR within the defined event selection criteria. As illustrated in Fig. 5.21, the maximum SNR achieved is over 40 in Run 3671, with the corresponding selection param-

eters summarized in Table 5.4.

Table 5.4 **The parameters when get highest SNR**

Parameters	Selection
Coincident distance (dR,m)	$< 5\,\mathrm{m}$
Energy related (n_{20})	> 35
AIC criteria (δA)	< -10
LE criteria (LE)	< 39
Goodness (G_{vd})	> 0.12

Similarly, as shown in Fig. 5.22 and 5.23, when operating at maximum SNR, the distributions of prompt and delayed signals remain consistent with expectations, and neutron capture lifetime fitting demonstrates excellent agreement with reference values.

As shown in Fig. 5.24, all 14 calibration runs demonstrate robust SNR performance. However, the calibrations on February 7-th exhibit significantly smaller statistical uncertainties due to higher neutron detection efficiency, resulting in substantially greater data volume for analysis.

5.2.3 The balance between neutron detection efficiency and SNR

Based on these results, we observe the relationship between SNR and neutron detection efficiency, as shown in Fig. 5.25. The maximum achievable efficiency exceeds $10\,\%$, while the SNR is lower than 20. This demonstrates a fundamental trade-off: stringent selection criteria yield excellent SNR at the cost of reduced efficiency, whereas relaxed cuts achieve high neutron detection efficiency but introduce significant background contamination.
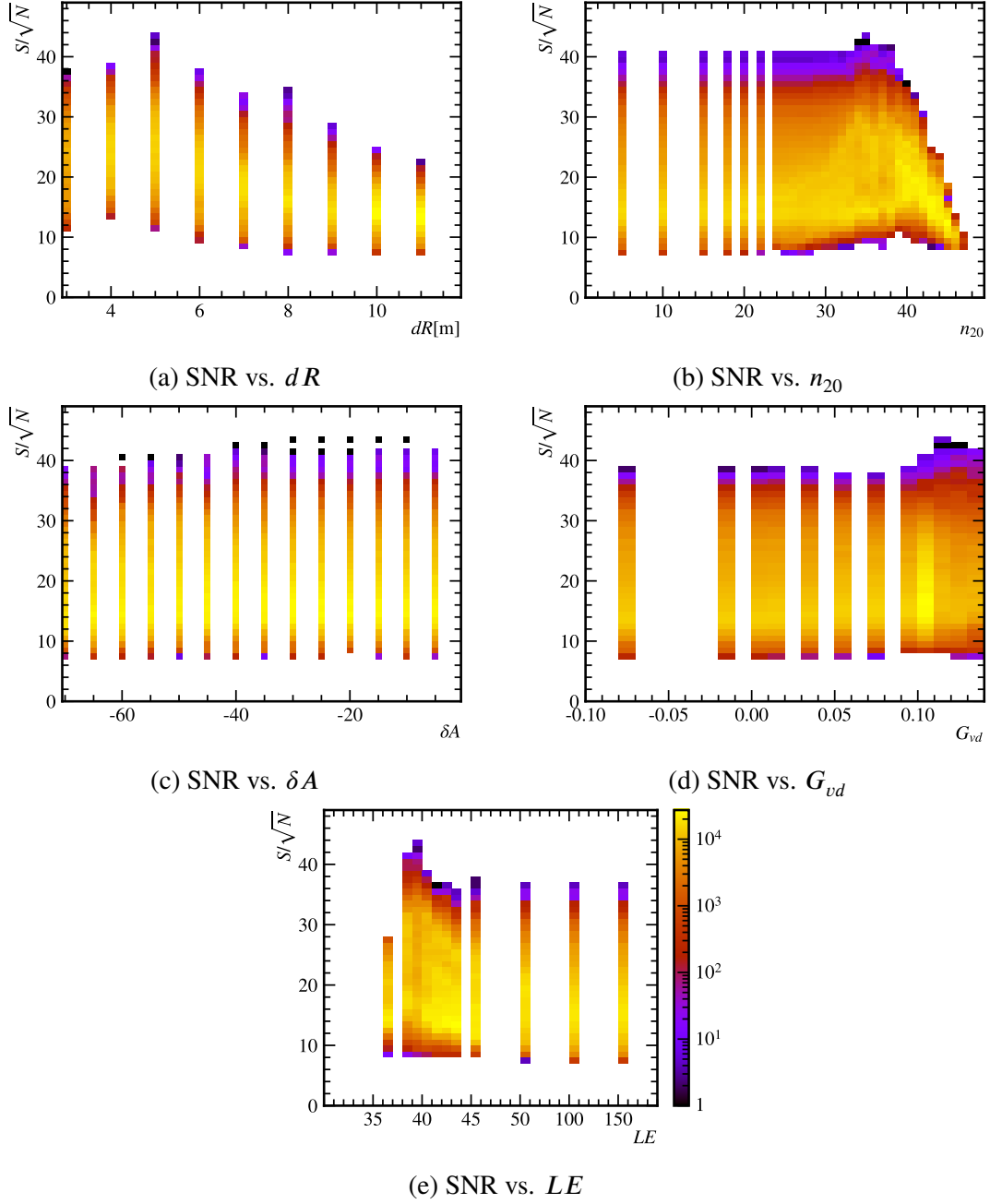
(a) SNR vs. dR

(b) SNR vs. n_{20}

(c) SNR vs. δA

(d) SNR vs. G_{vd}

(e) SNR vs. LE

Figure 5.21   Neutron detection SNR as a function of five key selection parameters in Run 3671. The maximum SNR achieved is over 40.

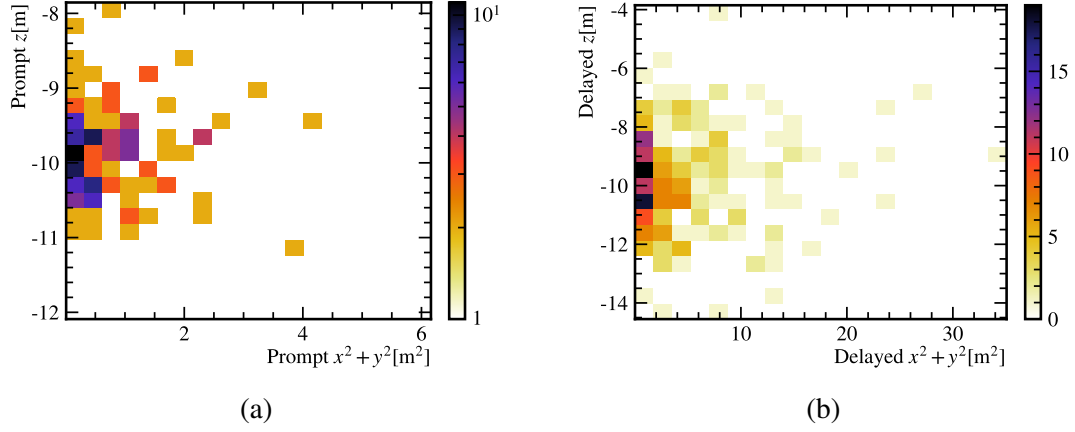(a)   (b)

Figure 5.22   The position distribution when getting the highest SNR in Run 3671. ((a)) is the position distribution of the prompt signals, and ((b)) is of the delayed signals.
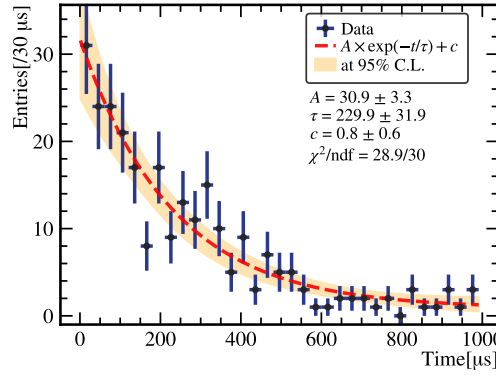

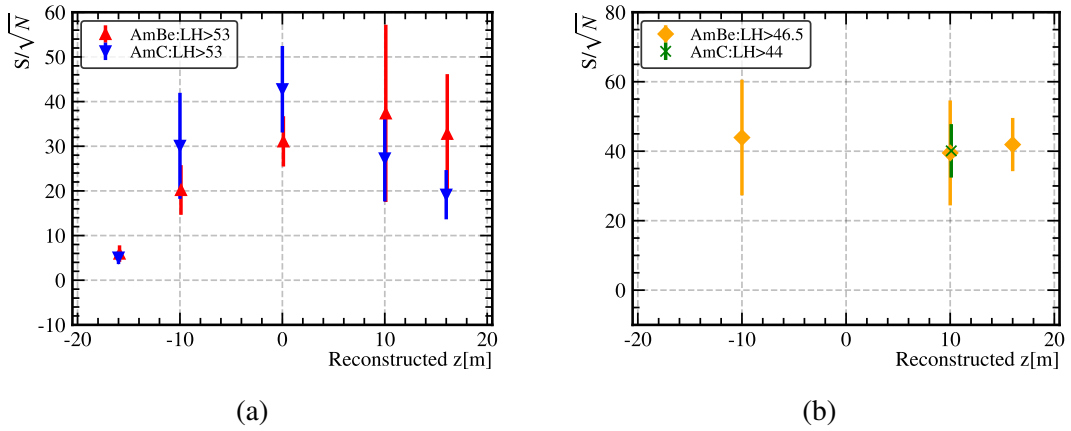Figure 5.23   The lifetime fit when getting the highest SNR in Run 3671.

(a)   (b)

Figure 5.24   The final highest neutron detection SNR in all 14 calibration runs. ((a)) is the result of calibrations on February 2-nd, and ((b)) is of calibrations on February 7-th.
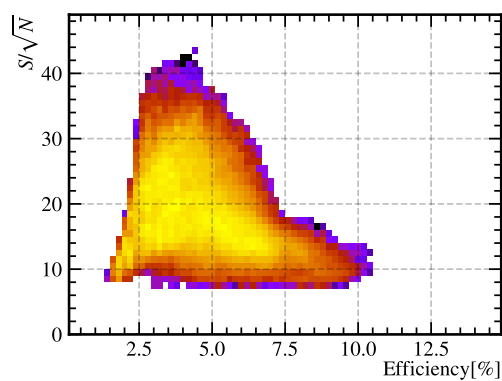
Figure 5.25 The relationship between SNR and neutron detection efficiency. The maximum efficiency exceeds 10 %, and the maximum SNR surpasses 40.

CHAPTER 6 THE MEASUREMENT OF SPALLATION NEUTRON YIELD IN WATER PHASE

From Sec. 5.1, we have demonstrated JUNO's neutron detection capability during its water phase. In the absence of calibration sources, this capability enables the detection of spallation neutrons produced by cosmic-ray muons traversing the detector. Because of the MM trigger threshold, we just use Run 3639 (around 2 h) and 3677 (around 5 h) for this measurement.

6.1 The reconstruction of muon track

Our muon reconstruction comes from Machine Learning (JUNO-doc-13818), based on Global trigger data, around 7 h. To better characterize muon properties, we define the following parameters, as shown in Fig. 6.1.

- D_{tc}: Distance from the CD center to the muon track
- L_t: Track length $L_t = 2 \times \sqrt{R_{CD}^2 - D_{tc}^2}, R_{CD} = 17.7\,\text{m}$
- Distance from events to muon track: dR

From the distribution of D_{tc}^2 as shown in Fig. 6.2(a), we observe cosmic-ray muons uniformly traversing the Central Detector. The Total PE distribution reveals that the majority of muons deposit between 10^5 and 10^6 PE, while a small fraction exhibit total PE counts below 10^5, as evidenced in Fig. 6.2(b). Fig. 6.2(c) demonstrates a strong correlation between muon track length and total PE for primary muons, forming a concentrated distribution band. However, events with $< 10^5$ PE despite long reconstructed tracks likely originate from PMT flasher artifacts or electronic noise mimicking muon signals. Therefore, we implement a selection cut requiring muon candidates to have total PE $> 10^5$. After the cut of $D_{tc} < 17.7\,\text{m}$ and Total PE $> 10^5$, the muon event rate is 4.03 Hz, which is consistent with the result of simulation $(0.004\,\text{Hz/m}^2)$[54]. Also from simulation[54], the average energy of muon is 207 GeV.

6.2 The search for spallation neutron

Similar to Sec. 5.1.3.1, we also use coincident reconstruction for spallation neutron, as shown in Fig. 6.3. For accidental coincident backgrounds, we reconstruct all events
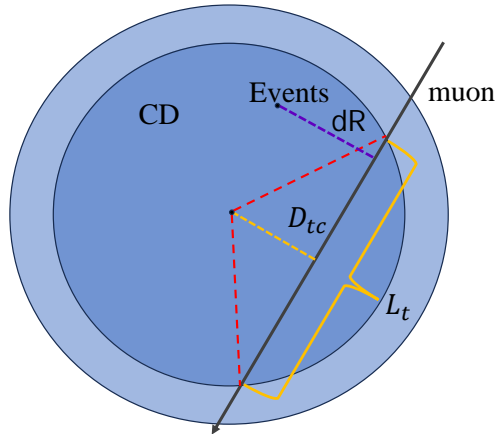
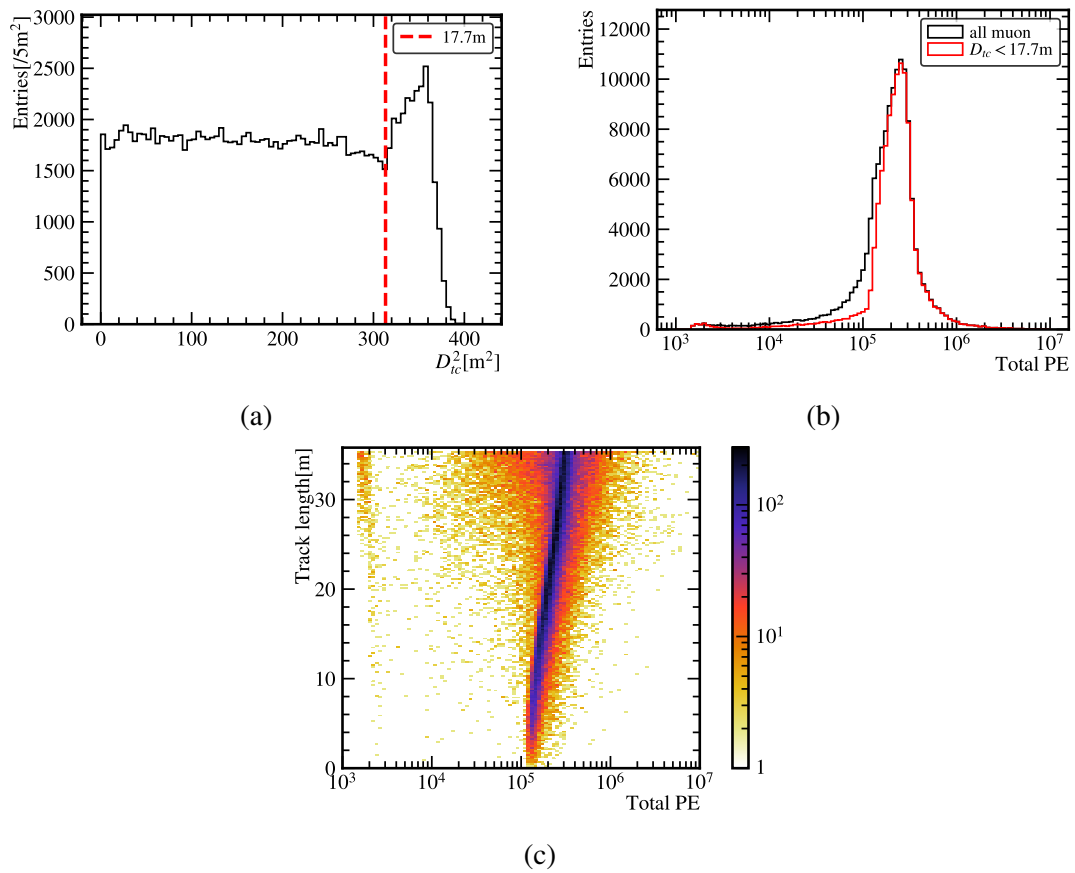Figure 6.1   The defination of parameters used in spallation neutron search.

(a)

(b)

(c)

Figure 6.2   ((a)) shows the distribution of D_{tc}^2, ((b)) evidences the total PE of muons and ((c)) demonstrates the relationship between total PE and the track length of muons.

in 20–2000 us after muons. In 0–20 us, events are influenced by baseline, after-pulse and Michel electrons, and would not be included in our study.
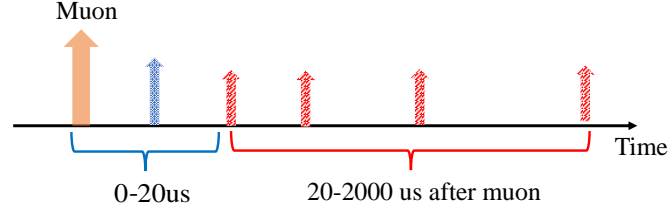

Figure 6.3   The coincident reconstruction of spallation neutrons

Validated through AmBe and AmC calibration, we get some basic cut for spallation neutrons:

- Fiducial volume: $r < 16$ m
- Background cut: $\delta A < -60$, $LE < 50$, $G_{vd} > 0.1$
- Energy related: $n_{20} < 70$

After applying basical cuts, we observe residual downward events clustered near the detector center, as illustrated in Fig. 6.4. To suppress this unknown background component, we implement an additional directional cut based on reconstructed direction $p_z/p > -0.75$.
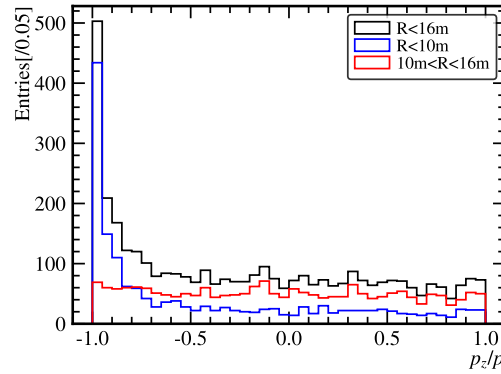

Figure 6.4   The coincident reconstruction of spallation neutrons

For the coincident distance and energy cut, we choose the events in 50–650 us as signals and in 1400–2000 us as background. After background subtraction, the distribution of dR reveals significant event clustering within 6 m, as evidenced in Fig. 6.5. This observation justifies implementing a position correlation cut of $dR < 6$ m to isolate true spallation neutron capture events. Similarly, in the n_{20} distribution after background subtraction as shown in Fig. 6.6, we observe a prominent peak around 35 PE. Using Gaussian fitting, the measured peak position is 36.3 PE. This contrasts with the expected value of

41 PE from that in calibration sources and the light-yield curve estimation of 38.9 PE. The primary reason for this discrepancy lies in the calibration sources measuring light yield at fixed positions, whereas the current result represents the average PE expectation within 16 m across the detector. Despite the numerical difference, these results remain consistent within the context of detector-scale estimation. Finally, we decide to use a cut of energy: $30 < n_{20} < 70$.
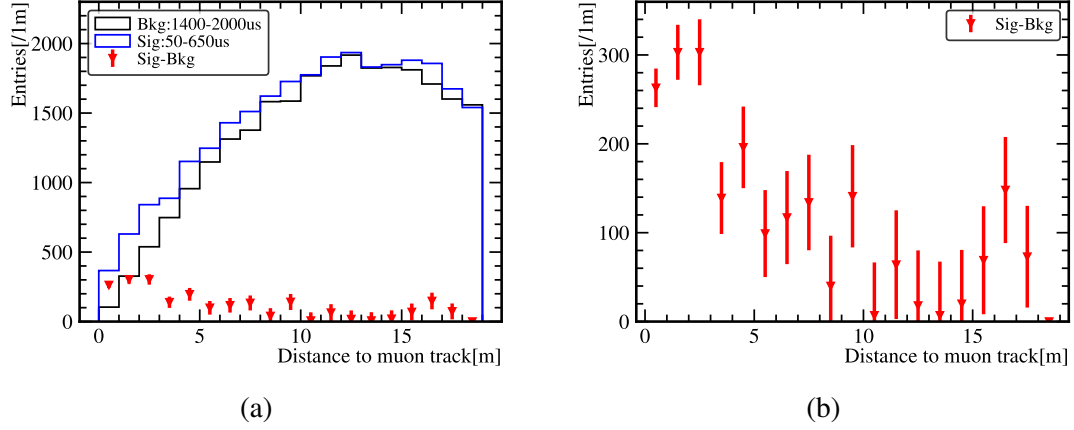

(a)	(b)

Figure 6.5   The coincident distance distribution.
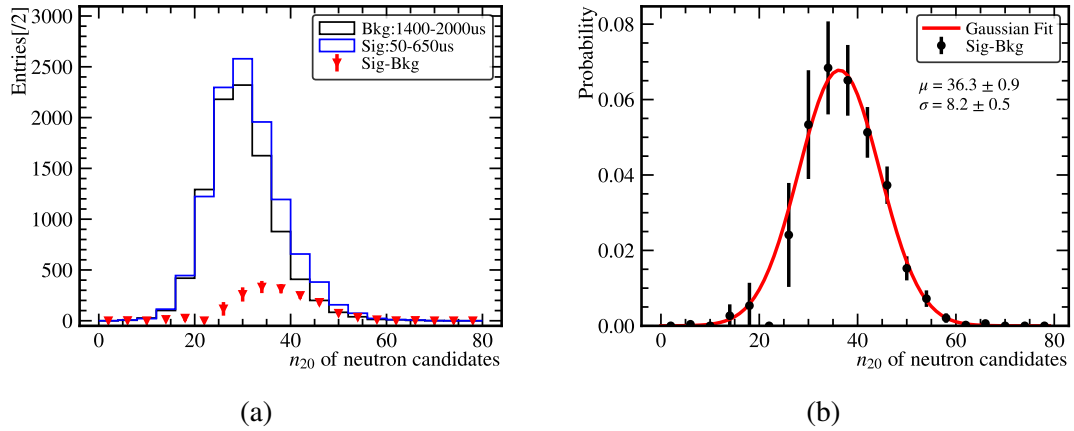

(a)	(b)

Figure 6.6   The distribution of energy related parameter n_{20}

At this stage, we calculate the number of spallation neutrons using capture lifetime fitting in [30, 930 us], as shown in Fig. 6.7. From the fit result, 987 ± 119 spallation neutron events are selected. We similarly examine the position distribution of selected events. By using coincidences within the 1100–2000 us window as background and subtracting them. In both background and selected events, we observe event clustering at the detector center. After background subtraction, we obtain the position distribution of spallation neutrons. The position distribution in the upper hemisphere of the detector exceeds that in the lower hemisphere. This asymmetry aligns with the detector non-uniformity observed during
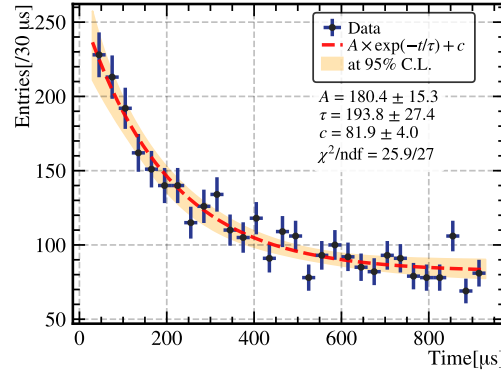
calibration source studies.

Figure 6.7   The lifetime fitting of spallation neutron.
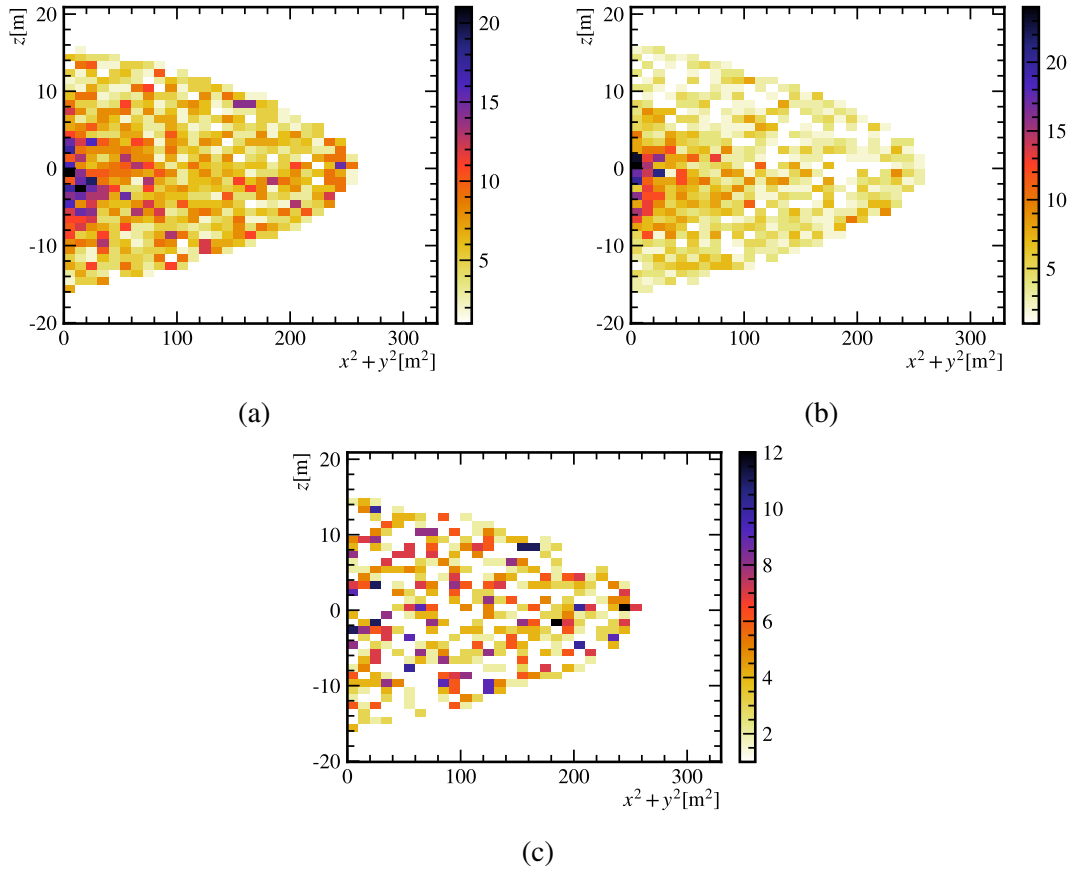

(a)

(b)

(c)

Figure 6.8   The position distribution. ((a)) evidences the distribution of the selected events. ((a)) shows the distribution of the background events in 1100–2000 us after muon. ((c)) displays the result of histogram subtraction between two distributions

6.3 The spallation neutron yield calibration

By combining data from the previous 14 calibration runs, we can estimate the average neutron detection efficiency within a 16-meter radius of the detector. We employed an R^3-weighted position averaging method to compute the position-dependent neutron detection

efficiency, yielding a volume-averaged efficiency of $3.3 \pm 0.4\,\%$, and the final efficiencies in our study are in Table. 6.1. The spallation neutron yield Y_n is defined as the neutron production rate per unit muon track length and per unit density, as defined in Eq. (6.1).

$$Y_n = \frac{N_n}{\rho N_{muon} L_{t,ave}} = \frac{N_n}{\rho \Sigma_{muon} L_t} \tag{6.1}$$

Only consider the statistical uncertainty, the spallation neutron yield is $Y_n = (2.31 \pm 0.41(\text{stat.})) \times 10^{-4}\ ^{-1}\text{g}^{-1}\text{cm}^2$.

Table 6.1   **The efficiencies in spallation neutron search**

	Effieciency
Neutron Tag	$3.3 \pm 0.4\,\%$
Fiducial volume	$73.9\,\%$
Coincident time window	$85.4\,\%$
Direcition cut	$87.5\,\%$

Simultaneously, there are three primary sources of systematic uncertainty. The first kind comes from the muon track reconstruction. We found a systematic $0.2\,\%$ bias between reconstructed muon track lengths and their true values, as shown in Fig. 6.9. Consequently, we attribute a $0.2\,\%$ systematic uncertainty to muon track reconstruction in our analyses. The second source of systematic uncertainty originates from neutron count variations induced by coincident distance selection. We perform parameter scans across multiple coincidence distances, as evidenced in Fig. 6.10 and quantified the systematic uncertainty using the maximum deviation from the central value obtained at different coincident distances. The final source of systematic uncertainty stems from detector inhomogeneity and discrepancies between simulation and experimental data. During AmBe and AmC calibrations, the neutron detection efficiency at $z = -16\,\text{m}$ approaches zero, as shown in Fig. 6.11(a). To quantify the impact of this local efficiency anomaly on the global average efficiency, we perform a parameter scan across a 5σ range of efficiency uncertainty (0 to $1.2\,\%$) based on the fitting results at this position. The range in the resulting detection efficiency is then adopted as the systematic uncertainty, as shown in Fig. 6.11(b). All the systematic efficiencies are summarized in Table. 6.2. Our final result of spallation neutron yield measurement is $Y_n = (2.31 \pm 0.22(\text{sys.}) \pm 0.41(\text{stat.})) \times 10^{-4}\ ^{-1}\text{g}^{-1}\text{cm}^2$. As shown in Fig. 6.12, our measurements in the water phase demonstrate statistically significant consistency with Super-Kamiokande's benchmark results across key neutron

detection parameters, validating the calibration methodology and detector performance.
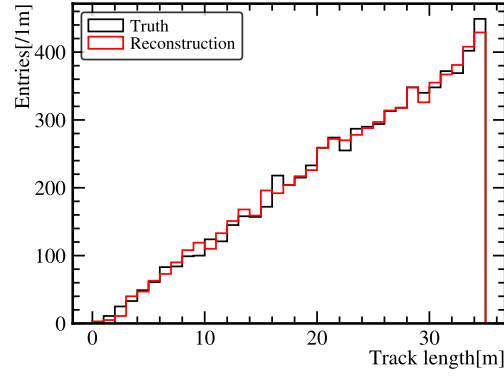

Figure 6.9   The track length distribution of reconstructed muon and their truth.
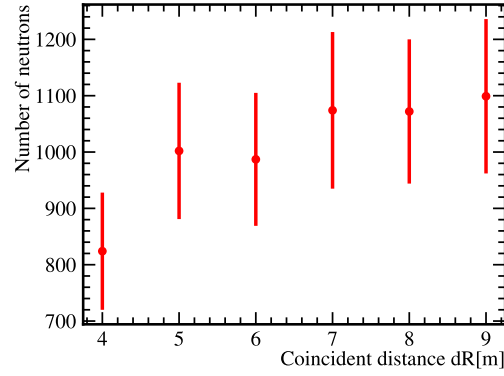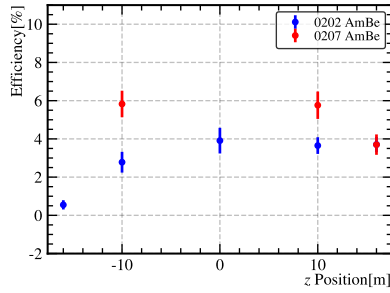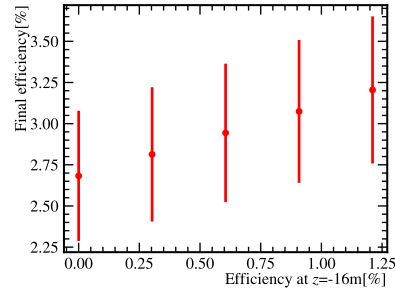

Figure 6.10   We scan dR from in 3–9 m, and calculate the number of neutrons.

Figure 6.11   The estimation of uncertainty from efficiency. ((a)) evidences the efficiency estimated from AmBe calibration with the same selection of spallation neutron. ((b)) shows that the final efficiency is influenced by the efficiency at $z = -16\,\mathrm{m}$.

Table 6.2   **The systematic uncertainty in spallation neutron search**

	uncertainty
Muon track reconstruction	0.2 %
Number of spallation neutrons	±92
The detection efficiency	±0.3 %
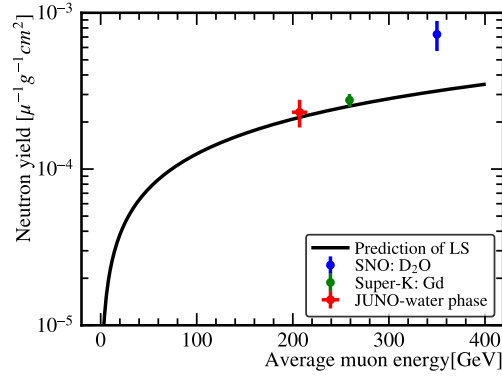
Figure 6.12   The final yield measurement. The result of SK comes from[55], and of SNO comes from[56].

6.3.1 Cross check using water-pool reconstructed muon

In order to cross-check the muon reconstruction in the water phase, we repeat the analysis using the water pool muon reconstruction method (JUNO-doc-13604). Except for the removal of the muon selection cut, all other selection criteria remain identical to those applied when using CD muons. The final result is $Y_n = (2.32 \pm 0.19(\text{sys.}) \pm 0.44(\text{stat.})) \times 10^{-4} \, ^{-1}\text{g}^{-1}\text{cm}^2$, as shown in Fig. 6.13 and 6.14. Those two results are consistent with each other.
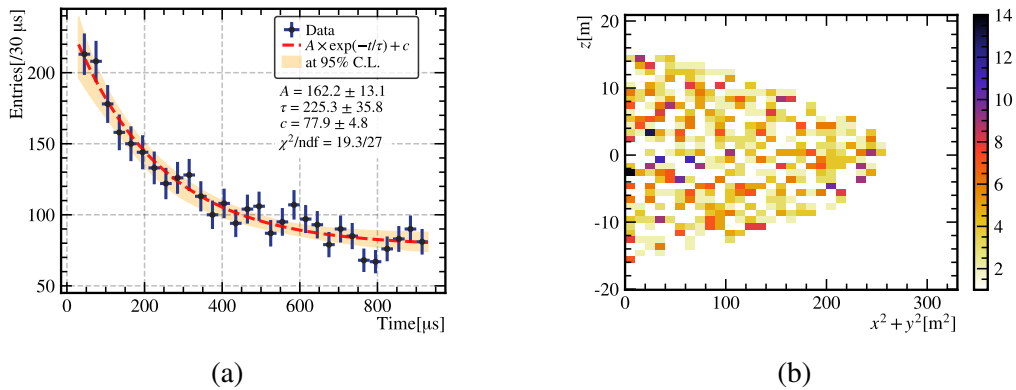

(a)

(b)

Figure 6.13   ((a)) is the lifetime fitting of spallation neutrons using the WP muons. ((b)) is the position distribution after extracting background.
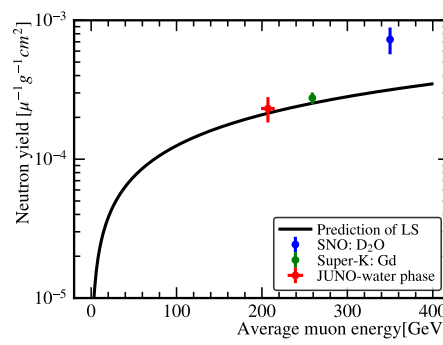
Figure 6.14   The measured spallation neutron yield using WP muon reconstruction.

CHAPTER 7 THE OBSERVATION OF SOLAR NEUTRINO

REFERENCES

[1] Breitenberger E. Scintillation spectrometer statistics[J]. Progress in nuclear physics, 1955, 4: 56-94.

[2] Chen L, et al. Optimization of the electron collection efficiency of a large area MCP-PMT for the JUNO experiment[J/OL]. Nucl. Instrum. Meth. A, 2016, 827: 124-130. https://www.scie ncedirect.com/science/article/pii/S0168900216303308. DOI: https://doi.org/10.1016/j.nima.2 016.04.100.

[3] Bellamy E, et al. Absolute calibration and monitoring of a spectrometric channel using a photo-multiplier[J/OL]. Nucl. Instrum. Meth. A, 1994, 339(3): 468-476. https://www.sciencedirect. com/science/article/pii/016890029490183X. DOI: https://doi.org/10.1016/0168-9002(94)901 83-X.

[4] Tao S X, et al. Secondary electron emission materials for transmission dynodes in novel photo-multipliers: A review[J]. Materials, 2016, 9(12): 1017.

[5] Furman M, Pivi M. Probabilistic model for the simulation of secondary electron emission[J]. Physical review special topics-accelerators and beams, 2002, 5(12): 124404.

[6] Bruining H, De Boer J. Secondary electron emission: Part I. Secondary electron emission of metals[J]. Physica, 1938, 5(1): 17-30.

[7] Ushio Y, et al. Secondary electron emission studies on MgO films[J]. Thin Solid Films, 1988, 167(1-2): 299-308.

[8] Jokela S J, et al. Secondary Electron Yield of Emissive Materials for Large-Area Micro-Channel Plate Detectors: Surface Composition and Film Thickness Dependencies[J]. Physics Procedia, 2012, 37: 740-747.

[9] Olano L, Montero I. Energy spectra of secondary electrons in dielectric materials by charging analysis[J/OL]. Results in Physics, 2020, 19: 103456. https://www.sciencedirect.com/science/ article/pii/S2211379720319173. DOI: https://doi.org/10.1016/j.rinp.2020.103456.

[10] Mane A U, et al. An Atomic Layer Deposition Method to Fabricate Economical and Robust Large Area Microchannel Plates for Photodetectors[J]. Physics Procedia, 2012, 37: 722-732.

[11] Guo L, et al. Effects of secondary electron emission yield properties on gain and timing perfor-mance of ALD-coated MCP[J]. Nucl. Instrum. Meth. A, 2021, 1005: 165369.

[12] Nathan R, Mee C. The energy distribution of photoelectrons from the K2CsSb photocathode [J/OL]. physica status solidi (a), 1970, 2(1): 67-72. https://api.semanticscholar.org/CorpusID: 97164824.

[13] Zhang A, et al. Performance evaluation of the 8-inch MCP-PMT for Jinping Neutrino Experi-ment[J/OL]. Nucl. Instrum. Meth. A, 2023, 1055: 168506. DOI: 10.1016/j.nima.2023.168506.

[14] Zhu Y, et al. The mass production and batch test result of 20" MCP-PMTs[J/OL]. Nucl. Instrum. Meth. A, 2020, 952: 162002. https://www.sciencedirect.com/science/article/pii/S016890021 9303833. DOI: https://doi.org/10.1016/j.nima.2019.03.057.

[15] Matsuoka K. Development and production of the MCP-PMT for the Belle II TOP counter[J/OL]. Nucl. Instrum. Meth. A, 2014, 766: 148-151. https://www.sciencedirect.com/science/article/pii/S0168900214005026. DOI: https://doi.org/10.1016/j.nima.2014.05.003.

[16] Krauss S, et al. Performance of the most recent Microchannel-Plate PMTs for the PANDA DIRC detectors at FAIR[J/OL]. Nucl. Instrum. Meth. A, 2023, 1057: 168659. https://www.sciencedirect.com/science/article/pii/S0168900223006496. DOI: https://doi.org/10.1016/j.nima.2023.168659.

[17] Cao Z, et al. Upgrading Plan Towards Multi-messenger Observation with LHAASO[J/OL]. EPJ Web of Conferences, 2019. https://api.semanticscholar.org/CorpusID:181399433.

[18] Kishimoto N, et al. Lifetime of MCP-PMT[J/OL]. Nucl. Instrum. Meth. A, 2006, 564(1): 204-211. https://www.sciencedirect.com/science/article/pii/S0168900206006991. DOI: https://doi.org/10.1016/j.nima.2006.04.089.

[19] Lehmann A, et al. Latest Technological Advances with MCP-PMTs[J]. J. Phys.: Conf. Ser., 2022, 2374(1): 012128.

[20] Cao W, et al. Secondary electron emission characteristics of the Al2O3/MgO double-layer structure prepared by atomic layer deposition[J/OL]. Ceramics International, 2021, 47(7): 9866-9872. DOI: 10.1016/j.ceramint.2020.12.128.

[21] Zhang Z, et al. Effect of Al2O3/MgO Composite Layer on the Properties of Microchannel Plate [J]. Surface Technology, 2021, 50(6): 199-205.

[22] Abusleme A, et al. Mass testing and characterization of 20-inch PMTs for JUNO[J]. The European Physical Journal C, 2022, 82(12): 1168.

[23] Orlov D, et al. High collection efficiency MCPs for photon counting detectors[J/OL]. JINST, 2018, 13(01): C01047. DOI: 10.1088/1748-0221/13/01/C01047.

[24] Zhang H, et al. Gain and charge response of 20" MCP and dynode PMTs[J]. JINST, 2021, 16 (08): T08009.

[25] Yang Y, et al. MCP performance improvement using alumina thin film[J]. Nucl. Instrum. Meth. A, 2017, 868: 43-47.

[26] Tan H H. A statistical model of the photomultiplier gain process with applications to optical pulse detection[J/OL]. The Telecommunications and Data Acquisition Report, 1982. http://hdl.handle.net/10150/612894.

[27] Bartlett M S, Harris T E. The Theory of Branching Processes[M/OL]. Springer Berlin, 1963. https://api.semanticscholar.org/CorpusID:90485223.

[28] Woodward P M. A statistical theory of cascade multiplication[J/OL]. Mathematical Proceedings of the Cambridge Philosophical Society, 1948, 44(3): 404-412. DOI: 10.1017/S0305004100024403.

[29] Prescott J. A statistical model for photomultiplier single-electron statistics[J]. Nuclear Instruments and Methods, 1966, 39(1): 173-179.

[30] Kalousis L. Calibration of the Double Chooz detector and cosmic background studies[D]. University of Strasbourg, 2012.

[31] Kalousis L, et al. A fast numerical method for photomultiplier tube calibration[J]. JINST, 2020, 15(03): P03023.

[32] Bruining H. Physics and applications of secondary electron emission[M]. Pergamon Press, 1954.

[33] Baroody E. A theory of secondary electron emission from metals[J]. Physical Review, 1950, 78(6): 780.

[34] Dekker A, Van der Ziel A. Theory of the production of secondary electrons in solids[J]. Physical Review, 1952, 86(5): 755.

[35] Wolff P A. Theory of secondary electron cascade in metals[J/OL]. Phys. Rev., 1954, 95: 56-66. https://link.aps.org/doi/10.1103/PhysRev.95.56.

[36] Kanaya K, et al. Secondary electron emission from insulators[J/OL]. J. Phys. D: Appl. Phys., 1978, 11(17): 2425. https://dx.doi.org/10.1088/0022-3727/11/17/015.

[37] Vaughan J. A new formula for secondary emission yield[J/OL]. IEEE Transactions on Electron Devices, 1989, 36(9): 1963-1967. DOI: 10.1109/16.34278.

[38] Luo F J, et al. Design & Optimization of the HV divider for JUNO 20-inch PMT[A]. 2023.

[39] Nelson, Rick. High-Definition Oscilloscopes Optimize Vertical Resolution[J/OL]. EE-Evaluation Engineering Online, 2016[Aug. 31, 2016]. https://www.electronicdesign.com/tec hnologies/test-measurement/article/21206728/high-definition-oscilloscopes-optimize-vertica l-resolution.

[40] Xu D, et al. Towards the ultimate PMT waveform analysis for neutrino and dark matter experiments[J/OL]. JINST, 2022, 17(06): P06040. https://dx.doi.org/10.1088/1748-0221/17/06/P0 6040.

[41] Wang Y, et al. The Fast Stochastic Matching Pursuit for Neutrino and Dark Matter Experiments [A]. 2024. arXiv: 2403.03156.

[42] Gagunashvili N D. Comparison of weighted and unweighted histograms[J]. Statistics, 2012: 43-44.

[43] Gelman A, Hill J. Analytical methods for social research: Data Analysis Using Regression and Multilevel/Hierarchical Models[M]. Cambridge University Press, 2006.

[44] Cowan G. Statistical Data Analysis[M]. Illustrated edition ed. Oxford: New York: Oxford University Press, 1997.

[45] Chen P, et al. Photoelectron backscattering in the microchannel plate photomultiplier tube[J]. Nucl. Instrum. Meth. A, 2018, 912: 112-114.

[46] Beck A H. Physical Electronics: Handbook of Vacuum Physics[M]. Elsevier, 1966.

[47] Jorgensen B. The Theory of Dispersion Models[M/OL]. Taylor & Francis, 1997. https://book s.google.co.jp/books?id=0gO7bgs_eSYC.

[48] Fukuda S, Y. Fukuda E I, T. Hayakawa, et al. The Super-Kamiokande detector[J/OL]. Nuclear Instruments and Methods in Physics Research Section A: Accelerators, Spectrometers, Detectors and Associated Equipment, 2003, 501(2): 418-462. https://www.sciencedirect.com/scienc e/article/pii/S016890020300425X. DOI: https://doi.org/10.1016/S0168-9002(03)00425-X.

[49] Patterson R, Laird E, Liu Y, et al. The extended-track event reconstruction for MiniBooNE [J/OL]. Nuclear Instruments and Methods in Physics Research Section A: Accelerators, Spectrometers, Detectors and Associated Equipment, 2009, 608(1): 206-224. https://www.scienced irect.com/science/article/pii/S0168900209012480. DOI: https://doi.org/10.1016/j.nima.2009. 06.064.

[50] Jiang M, Abe K, Bronner, et al. Atmospheric neutrino oscillation analysis with improved event reconstruction in super-kamiokande iv[J/OL]. Progress of Theoretical and Experimental Physics, 2019, 2019(5): 053F01. https://doi.org/10.1093/ptep/ptz015.

[51] Liu X, Dou W, Xu B, et al. First-principle event reconstruction by time-charge readouts for TAO [J/OL]. Eur. Phys. J. C, 2025, 85(4): 438. DOI: 10.1140/epjc/s10052-025-14161-6.

[52] Yu P, et al. Multi-threaded Simulation Software for the JUNO Experiment[A]. 2025. arXiv: 2503.20219.

[53] Dou W, Xu B, Zhou J, et al. Reconstruction of point events in liquid-scintillator detectors subjected to total internal reflection[J/OL]. Nucl. Instrum. Meth. A, 2023, 1057: 168692. DOI: 10.1016/j.nima.2023.168692.

[54] JUNO physics and detector[J/OL]. Progress in Particle and Nuclear Physics, 2022, 123: 103927. https://www.sciencedirect.com/science/article/pii/S0146641021000880. DOI: https://doi.org/ 10.1016/j.ppnp.2021.103927.

[55] Shinoki M, et al. Measurement of the cosmogenic neutron yield in Super-Kamiokande with gadolinium loaded water[J/OL]. Phys. Rev. D, 2023, 107(9): 092009. DOI: 10.1103/PhysRe vD.107.092009.

[56] Aharmim B, Ahmed S N, et al. Cosmogenic neutron production at the Sudbury Neutrino Observatory[J/OL]. Phys. Rev. D, 2019, 100: 112005. https://link.aps.org/doi/10.1103/PhysRev D.100.112005.